Contrib Mineral Petrol (2012) 164:551–569
DOI 10.1007/s00410-012-0748-2

ORIGINAL PAPER

U–Pb zircon dating, geochemical and Sr–Nd–Hf isotopic compositions of Early Indosinian intrusive rocks in West Qinling, central China: petrogenesis and tectonic implications

Biji Luo · Hongfei Zhang · Xinbiao Lü

Received: 16 December 2011 / Accepted: 6 April 2012 / Published online: 28 April 2012

Abstract The Qinling–Dabie–Sulu orogenic belt is the junction between the North and South China blocks, which resulted from the final amalgamation of China continents during the Indosinian. Indosinian granitoids are widespread in the Qinling orogen, and their geneses can thus constrain the evolution of China continent. We carried out a combined U–Pb zircon dating and geochemical study for the Shuangpengxi granodiorite pluton and the Xiekeng diorite–granodiorite pluton in the middle part of the West Qinling orogen. U–Pb zircon dating shows that the magma crystallization ages of 242 ± 3 Ma for the Shuangpengxi pluton and ~244–242 Ma for the Xiekeng pluton. Geochemical and Sr–Nd–Hf isotopic compositions reveal that the magma of the Shuangpengxi granodiorite was derived from partial melting of crustal materials. The Xiekeng diorites can be divided into high-Al diorite and high-Mg diorite. Both of them resulted from partial melting of enriched lithospheric mantle, but their mantle source had been modified by previous slab-derived melt. The high-Al diorite was formed by fractional crystallization of olivine, pyroxene and/or preferential accumulation of plagioclase, and the high-Mg diorite was formed by fractional crystallization of olivine and/or preferential accumulation of pyroxene. The Xiekeng granodioritic porphyry was formed by mixing of crust-derived and mantle-derived melts. We propose that the Early Indosinian magmatism resulted from break-off of subducted oceanic slab after collision. The slab break-off model can well explain the linear distribution of the Early Indosinian plutons and rapid crustal uplift during the Middle Triassic in the West Qinling.

Keywords Intrusive rock · U–Pb zircon dating · Geochemistry · Petrogenesis · Tectonic implication · West Qinling · China

Introduction

Mantle-derived mafic magma, emplaced at different crustal levels, can play an important role for the generation and evolution of granites (Huppert and Sparks 1988; Bergantz 1989; Annen and Sparks 2002; Kemp et al. 2007; Koteas et al. 2010). Mafic magma can act as parental magma, heat source and end-member of mixing or assimilation (Tepper et al. 1993; van de Flierdt et al. 2003). Annen et al. (2006, 2008) proposed a model of intermediate and silicic melt generation in Deep Hot Zone that was formed by repeatedly underplated or interplated mafic sills. The melt can be generated by incomplete crystallization of the mafic magma (residual melt), by partial melting of crustal rocks and by mixing between residual melt (or mafic magma) and crustal melt. The role of mafic magma for the origin of granitoids can be achieved in areas where granitoids are associated with gabbros, diorites, mafic dykes and mafic magmatic enclaves (Altherr et al. 1999; Bonin 2004; Tepper and Kuehner 2004; Barbarin 2005). Mantle-derived

---

Communicated by J. Hoefs.

Electronic supplementary material The online version of this article (doi:10.1007/s00410-012-0748-2) contains supplementary material, which is available to authorized users.

B. Luo · H. Zhang (✉)
State Key Laboratory of Geological Process and Mineral Resources and Faculty of Earth Sciences, China University of Geosciences, Wuhan 430074, People's Republic of China
e-mail: hfzhang@cug.edu.cn

X. Lü
Faculty of Resources, China University of Geosciences, Wuhan 430074, People's Republic of China

magma closely associated with crustal magma can be used to better constrain the lithosphere evolution and the geodynamic processes (Bonin 2004).

The Qinling orogen in central China separates the North China block from the South China block and links the Kunlun and Qilian orogens to the west and the Dabie–Sulu orogen to the east (Fig. 1a), which is an important tectonic domain in eastern Asia (Meng and Zhang 2000; Ratschbacher et al. 2003). The Qinling orogen can be divided into the East and West Qinling (Zhang et al. 2001; Feng et al. 2002). Previous studies focused mainly on the East Qinling and the neighboring northwestern margin of the Yangtze block and eastern part of the West Qinling. Geochronological and geochemical data show that most granitoids in

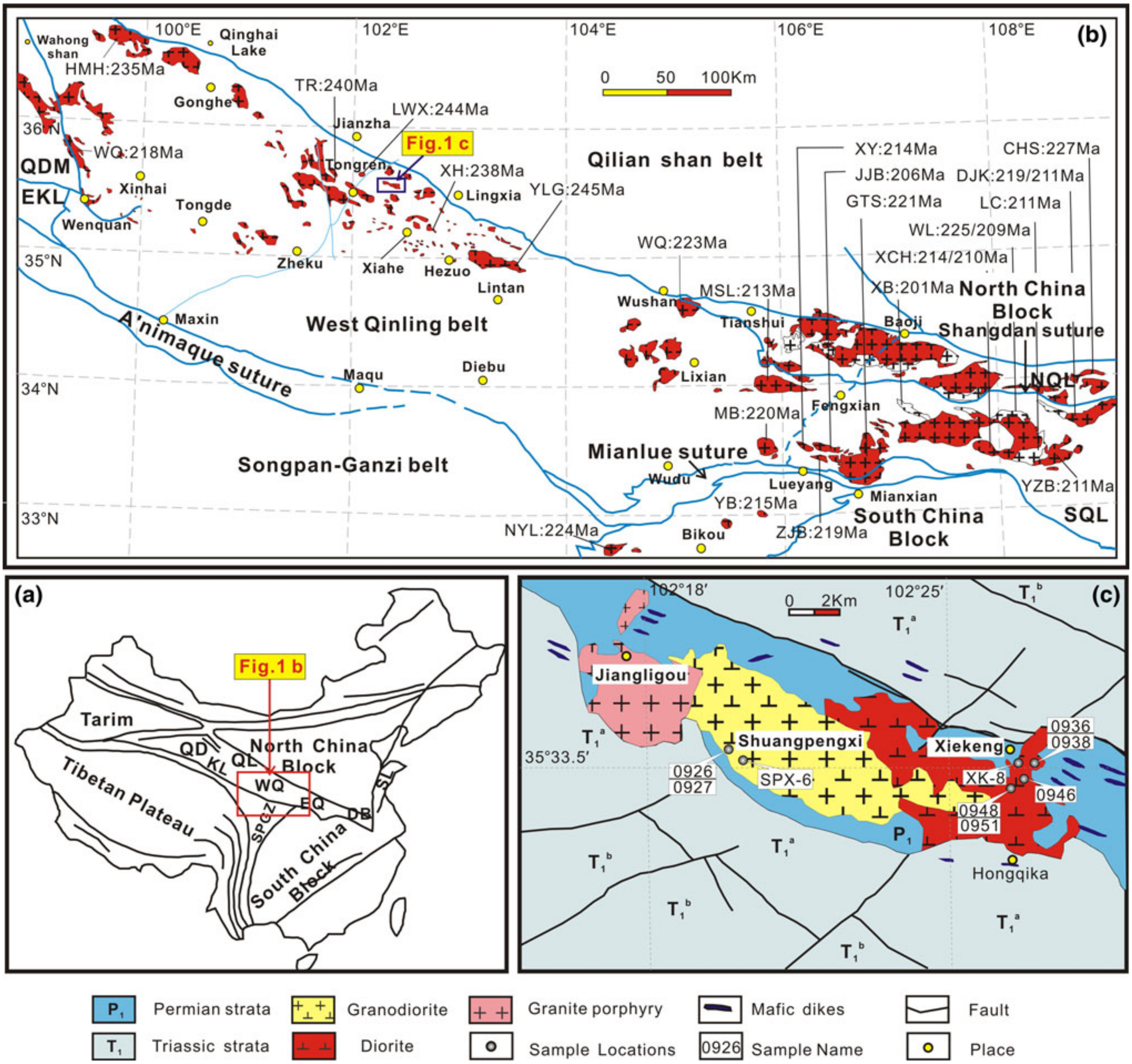

Fig. 1 **a** Simplified geological map of China, showing major tectonic units of China (after Zheng et al. 2010); **b** Simplified map showing distribution of the Early Mesozoic granitoids in the Qinling orogen (after Feng et al. 2002); and **c** Geological map of the Shuangpengxi area, West Qinling. Abbreviations in **a** and **b**: *WQ* West Qinling, *EQ* East Qinling, *SPGZ* Songpan-Ganzi terrane, *DB* Dabie belt, *SL* Sulu belt, *QD* Qaidam, *QL* Qilian Shan belt, *KL (EKL)* Kunlun Shan belt, *NQL* North Qinling, *SQL* South Qinling. Pluton names and zircon U–Pb age data sources in **b**: East Qinling (Sun et al. 2002; Qin et al. 2009, 2010b; Zhang et al. 2008 and references therein; Jiang et al. 2010); Northwestern margin of South China block (Li et al. 2007; Zhang et al. 2007b; Qin et al. 2008); Eastern part of the West Qinling (Sun et al. 2002; Qin et al. 2009; Cao et al. 2011): *MB* Miba, *MSL* Mishuling, *WQ* Wenquan, Middle part of the West Qinling (Feng et al. 2002; Jin et al. 2005; Wang et al. 2010): *YLG* Yeliguan, *XH* Xiahe, *LWX* Longwuxia, *TR* Tongren, Western part of the West Qinling (Zhang et al. 2006): *HMH* Heimahe, *WQ* Wenquan

the East Qinling and its neighboring areas have magma crystallization ages ranging from 227 to 205 Ma (Late Indosinian) and that they formed in a post-collisional setting (Sun et al. 2002; Zhang et al. 2007b, 2008; Qin et al. 2008, 2009, 2010a, b and references therein; Cao et al. 2011). However, recent study shows that some granitoids from the middle and western parts of the West Qinling have magma crystallization ages of ~245–235 Ma (Feng et al. 2002; Jin et al. 2005; Zhang et al. 2006; Wang et al. 2010), which are obviously older than those of the East Qinling granitoids. There are two competing tectonic models for the generation of the West Qinling granitoids: (1) active continental margin (Jin et al. 2005; Meng et al. 2005) and (2) early stage of post-collision setting (Zhang et al. 2006, 2008). Therefore, additional studies are required.

In this paper, we carry out an integrated study of U–Pb zircon dating, geochemical and Sr–Nd–Hf isotopic compositions for the Xiekeng (XK) diorite–granodiorite pluton and Shuangpengxi (SPX) granodiorite pluton in the middle part of the West Qinling orogen. The XK and SPX plutons provide an excellent opportunity to study the role of mafic magmas on the origin of granitoids and to examine the model of Deep Hot Zones (Annen et al. 2006, 2008). We also use these data to discuss their tectonic implications.

Geological backgrounds

The Qinling orogenic belt is a multistage orogenic belt and extends for more than 1,500 km in central China (Fig. 1a) (Meng and Zhang 2000; Ratschbacher et al. 2003). The East Qinling orogen is composed of three blocks and two sutures (Meng and Zhang 1999). The Shangdan suture zone separates the North China block (including the North Qinling) from the Qinling microplate (the South Qinling) (Fig. 1b). The North Qinling is predominantly composed of Proterozoic to Paleozoic medium-grade meta-sedimentary and meta-volcanic (Li et al. 1996; Zhang et al. 2001). The South Qinling consists mainly of Late Proterozoic to Triassic sediments overlying Neo-Proterozoic crystalline basement. The Triassic collision of the South China block with the South Qinling along the Mianlue suture led to the widespread fold-thrust deformation and granitic magmatism throughout the East Qinling (Zhang et al. 2001; Sun et al. 2002).

The West Qinling is bounded by the East Kunlun and Qaidam terranes along the Wenquan-Wahongshang fault to the west, separated from the Qilian orogen by the Qinghai Lake-Baoji fault to the north, and separated from the Bayan Har/Songpan-Garze block by the A'nimaque-Mianlue suture zone to the south (Fig. 1b). The A'nimaque-Mianlue suture zone along the southern margin of the Qinling orogenic belt contains abundant ophiolite fragments that record collision between the North and South China blocks, which is considered to be a Late Paleozoic Paleo-Tethys oceanic subduction zone dipping to the north (Li et al. 1996; Xu et al. 2002; Konstantinovskaia et al. 2003; Lai et al. 2008; Yang et al. 2009). In the West Qinling, sedimentary cover is mainly the Devonian to Cretaceous sediments and Precambrian basement is rarely exposed (Feng et al. 2002).

Granitoids are widespread in the West Qinling. Most of them have sharp contact with their wall-rock of the Phanerozoic sedimentary cover. The Mishuling, Miba, Wenquan and Wuduojinghua granitoid plutons in the eastern part of the West Qinling have U–Pb zircon ages of ~225–211 Ma (Fig. 1b) (Sun et al. 2002; Qin et al. 2009; Cao et al. 2011). The granitoids in the middle part have U–Pb zircon ages ranging from 245 to 238 Ma (Fig. 1b) (Feng et al. 2002; Jin et al. 2005; Wang et al. 2010). The granitoids in the western part of the West Qinling are located along the Wenquan-Wahongshan fault and the southern margin of the Qinghai Lake fault (Fig. 1b). They have U–Pb zircon ages of 235–218 Ma (Zhang et al. 2006).

In this paper, samples from the XK and SPX plutons in the middle part of the West Qinling were collected. The XK and SPX plutons intrude Permian and Early Triassic sediments (Fig. 1c). The XK pluton, with an area of ~14 km^2, comprises mainly diorite with minor granodioritic porphyry. In the field, no sharp contact between these rocks is observed, indicating that they could be coeval. The diorite is dark gray or gray green, medium grained, massive and consists of 3–5 % quartz, 60–75 % plagioclase, 5–15 % orthopyroxene, 5–8 % clinopyroxene, 3–5 % hornblende and biotite with minor Fe–Ti oxide, apatite and titanite. The hornblende and biotite mostly occur as thin rims on pyroxene (Fig. 2a, b). The granodioritic porphyry has a groundmass of fine-grained quartz and feldspar with minor biotite, and phenocrysts of plagioclase, biotite and hornblende (Fig. 2c). Accessory minerals include zircon, Fe–Ti oxide and apatite. The SPX granodiorite intrudes the XK pluton and occurs as a stock with an area of ~14 km^2 (Fig. 1c). This granodiorite is medium-coarse grained and massive and consists of 15–20 % quartz, 40–45 % plagioclase, 10–15 % K-feldspar, 5–8 % hornblende and 5–8 % biotite (Fig. 2d). Accessory minerals include apatite, magnetite and zircon.

Analytical methods

Fresh rock samples were crushed in a steel crusher and then powdered in an agate mill to a grain size <200 mesh. Major elements were analyzed at the Hubei Geological Analytical Center, Wuhan. For analytical methods see Zhang et al. (2002). The analytical uncertainty is generally <5 %. Trace elements, including REE, were measured using Agilent 7500a ICP-MS at the State Key Laboratory of Geological

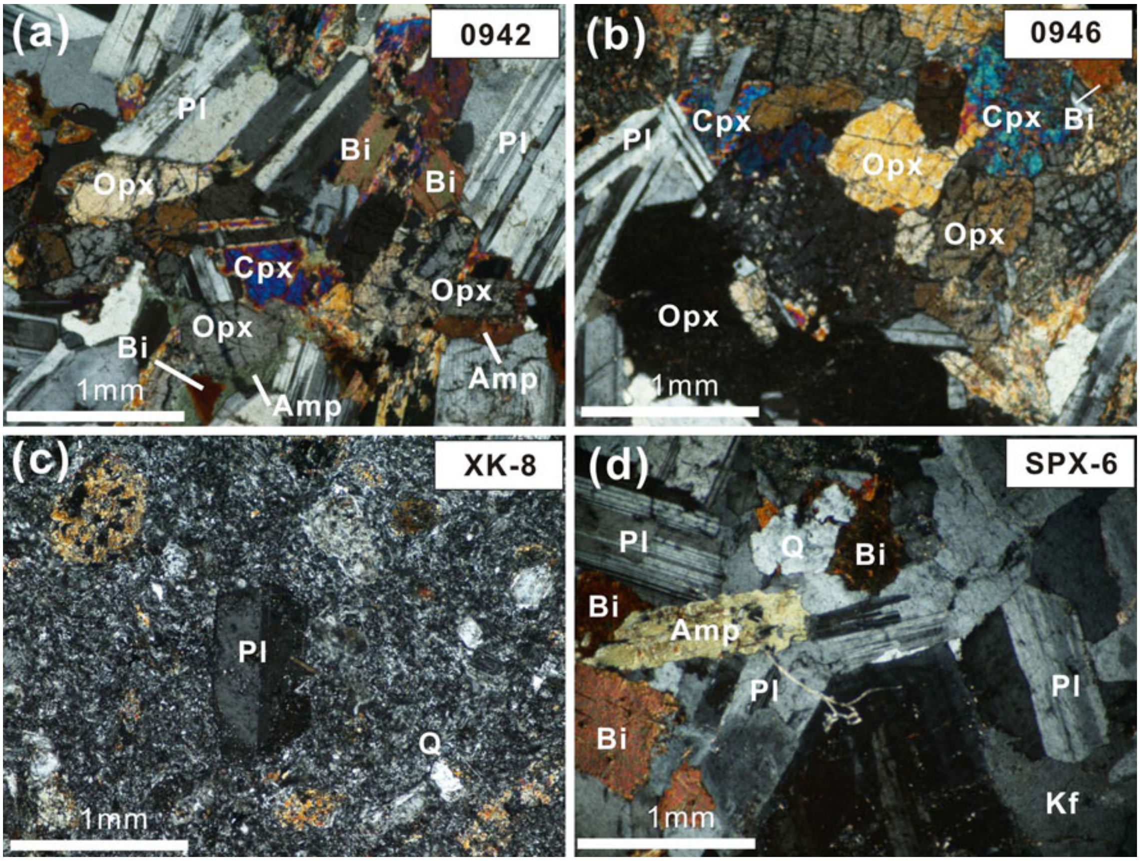

Fig. 2 Photomicrographs of representative samples of the intrusive rocks from West Qinling. XK pluton: **a** high-Al diorite (0942); **b** high-Mg diorite (0946); **c** granodioritic porphyry (XK-8); SPX pluton: **d** granodiorite (SPX-6). *Amp* amphibole, *Bt* biotite, *Opx* orthopyroxene, *Cpx* clinopyroxene, *Pl* plagioclase, *Kfs* K-feldspar, *Qz* quartz

Processes and Mineral Resources (GPMR), China University of Geosciences, Wuhan. Sample-digesting procedure for ICP-MS analyses and analytical precision and accuracy are the same as described by Liu et al. (2008).

Whole-rock Sr and Nd isotopic ratios were measured by a Triton thermal ionization mass spectrometer at GPMR. ^{87}Rb/^{86}Sr and ^{147}Sm/^{144}Nd ratios were calculated from Rb, Sr, Sm and Nd contents measured by ICP-MS. The measured Sr and Nd isotopic ratios were normalized to ^{86}Sr/^{88}Sr $= 0.1194$ and ^{146}Nd/^{144}Nd $= 0.7219$, respectively. During the period of analysis, NBS987 standard yielded an average ^{87}Sr/^{86}Sr value of 0.710239 ± 10 (2σ), and BCR-2 standard gave an average ^{143}Nd/^{144}Nd value of 0.512620 ± 2 (2σ). For details of the Sr and Nd isotopic analytical procedures see Gao et al. (2004).

Zircons were separated using conventional techniques. Zircons, selected by examination with a binocular microscope, were mounted in epoxy resin and polished to approximately half thickness. Cathodoluminescence (CL) images, taken at Northwest University, Xi'an, were used to check the internal textures of individual zircon and to guide U–Pb dating and Hf isotope analysis. U–Pb zircon dating was carried out using LA-ICP-MS on an Agilent 7500 equipped with a 193-nm ArF excimer laser at GPMR. Operating conditions are the same as described by Liu et al. (2010). A beam diameter of 32 μm was used for sample SPX-6 and XK-8 and 24 μm for sample 0951. Zircon 91500 and the GSE-1G glass were used as an external standard for Pb/U ratio and concentration, respectively. Common Pb correction is made by using the program of ComPbCorr#3-17 (Andersen 2002). Off-line selection and integration of background and analyte signals, and time-drift correction and quantitative calibration were conducted by *ICPMSDataCal* (Liu et al. 2010). The data were processed using the ISOPLOT program (Ludwig 2003).

Zircon Hf isotope analysis was carried out in situ using a Neptune MC-ICP-MS at GPMR. Analytical spots were located close to or on the top of LA-ICP-MS spots or in the same growth domain as inferred from CL images. The instrumental conditions and data acquisition were described by Hu et al. (2012). The analyses were conducted with a beam diameter of 44 μm, a hit rate of 8 Hz and laser energy of 60 mJ. A major problem to the accurate determination of the Hf isotopic composition of zircon using LA-MC-ICP-MS is to make the isobaric interference corrections of ^{176}Yb and ^{176}Lu on ^{176}Hf (Woodhead et al.

2004; Yuan et al. 2008; Kemp et al. 2009; Fisher et al. 2011). Recent studies have suggested that the Yb isotope abundances for the mass bias and isobaric interference correction may be instrument and/or technique specific (Kemp et al. 2009; Fisher et al. 2011). During this study, the mass fractionations of Hf and Yb were calculated using an exponential law and values of 0.7325 for ^{179}Hf/^{177}Hf and 1.1265 for ^{173}Yb/^{171}Yb, respectively (IUPAC 1991). The mass bias behavior of Lu is typically assumed to be similar to that of Yb, and βYb was determined using the ^{173}Yb/^{171}Yb measured during each zircon analysis (Woodhead et al. 2004). Isobaric interference of ^{176}Lu and ^{176}Yb on ^{176}Hf was monitoring by measuring the intensity of the interference-free ^{175}Lu and ^{173}Yb isotope, respectively. Ratios used for the corrections were ^{176}Lu/^{175}Lu = 0.02659 and ^{176}Yb/^{173}Yb = 0.79108, respectively (IUPAC 1991). Off-line selection and integration analyte signals, and isobaric interference and mass fractionation correction of Lu–Hf isotopic ratios were also performed by *ICPMS-DataCal* (Liu et al. 2010).

For most natural zircon samples that have relatively high ^{176}Yb/^{177}Hf ratio, the interference correction of ^{176}Yb on ^{176}Hf must be able to accommodate a wide range of ^{176}Yb/^{177}Hf ratios (Valley et al. 2010, Fisher et al. 2011). To monitor the accuracy of this correction, every 5–7 sample analyses were followed by analysis of the reference zircons. Reference zircons 91500 (^{176}Yb/^{177}Hf = 0.0069–0.0077), GJ-1 (^{176}Yb/^{177}Hf = 0.0057–0.0062), Mud Tank (^{176}Yb/^{177}Hf = 0.0009–0.0010) and Temora (^{176}Yb/^{177}Hf = 0.008–0.042) were analyzed as unknown (Table S1). During the analysis, the standard zircons gave ^{176}Hf/^{177}Hf ratios of 0.282309 ± 6 (2σ, MSWD = 0.68, n = 11) for 91500 and 0.282024 ± 8 (2σ, MSWD = 1.7, $n = 10$) for GJ-1 and 0.282500 ± 5 (2σ, MSWD = 0.72, $n = 7$) for Mud Tank and 0.282675 ± 7 (2σ, MSWD = 1.2, $n = 11$) for Temora, respectively. They are all well consistent with the recommended ^{176}Hf/^{177}Hf ratios of 0.282308 ± 6 (Blichert-Toft 2008) for 91500, 0.282015 ± 19 for GJ-1 (Elhlou et al. 2006), 0.282504 ± 26 for Mud Tank (Woodhead and Hergt 2005) and 0.282680 ± 24 for Temora (Woodhead et al. 2004) within analytical errors (Fig. S1), respectively. Most of the samples analyzed in this study have less ^{176}Yb/^{177}Hf ratio than our standards and do not display any obviously correlation between the ^{176}Hf/^{177}Hf and ^{176}Yb/^{177}Hf ratios (Fig. S1), indicating that our interference corrections are reasonable and the zircon Hf isotope data are accurate.

The decay constant for ^{176}Lu of 1.865×10^{-11} year^{-1} was adopted (Scherer et al. 2001). Initial ^{176}Hf/^{177}Hf ratio, denoted as $\varepsilon_{\mathrm{Hf}}(t)$, is calculated relative to the chondritic reservoir with a ^{176}Hf/^{177}Hf ratio of 0.282772 and ^{176}Lu/^{177}Hf of 0.0332 (Blichert-Toft et al. 1997). Single-stage Hf model ages (T_{DM1}) are calculated relative to the depleted mantle, which is assumed to have a linear isotopic growth from ^{176}Hf/^{177}Hf = 0.279718 at 4.55 Ga to 0.283250 at present, with ^{176}Lu/^{177}Hf ratio of 0.0384 (Vervoort and Blichert-Toft 1999), and two-stage Hf model ages (T_{DM2}) are calculated by assuming a mean ^{176}Lu/^{177}Hf value of 0.015 for the average continental crust (Griffin et al. 2002). The single-stage Hf model age (T_{DM1}) is taken for positive $\varepsilon_{\mathrm{Hf}}(t)$ values, and two-stage Hf model age (T_{DM2}) is taken for negative $\varepsilon_{\mathrm{Hf}}(t)$ values (Zheng et al. 2006).

Results

U–Pb zircon ages

LA-ICP-MS zircon U–Pb data are listed in the Table S2, and representative zircon CL images and their U–Pb concordia plots are shown in Figs. 3 and 4, respectively.

Zircons from the SPX granodiorite (sample SPX-6) are colorless, transparent and euhedral. Most of them are short to long prismatic, with length to width ratios ranging from 1:1 to 3.5:1. In CL images, these zircons have planar zoning or oscillatory zoning, consistent with a magmatic origin (Fig. 3a) (Corfu et al. 2003). Some zircons display inherited zircon cores with weak zoning or no zoning (Fig. 3a). Four analyses on the inherited cores give ^{206}Pb/^{238}U ages of 357 ± 5, 264 ± 4, 263 ± 4 and 261 ± 3 Ma, respectively (Fig. 4a). One analysis has a young age of 222 ± 4 Ma, probably due to the Pb loss (Fig. 4a). These analyses have 120–321 ppm U, 91.5–236 ppm Th and Th/U ratios of 0.57–0.78. Eighteen analyses on magmatic domains show 64.5–366 ppm U, 64–258 ppm Th and Th/U ratios of 0.67–1.51 (Table S2). They yield ^{206}Pb/^{238}U ages between 231 ± 4 and 251 ± 5 Ma, with a weighted mean of 242 ± 3 Ma (2σ; MSWD = 2.6) (Fig. 4a), which is interpreted to be the magma crystallization age of the SPX granodiorite.

Two samples from the XK granodioritic porphyry (sample 0951 and XK-8) were chosen for U–Pb zircon dating. Zircons from sample 0951 are colorless, transparent, short prismatic (up to 200 μm long) and euhedral or subhedral. CL images show no or weak zoning (Fig. 3b). Fourteen analyses show 162–786 ppm U, 93.5–641 ppm Th and Th/U ratios of 0.41–0.95 (Table S2). Among them, three analyses give ^{206}Pb/^{238}U ages of 270 ± 4, 264 ± 4 and 258 ± 4 Ma, respectively (Fig. 4b), and the remaining eleven analyses yielded ^{206}Pb/^{238}U ages ranging from 240 to 248 Ma, with a weighted mean of 244 ± 2 Ma (2σ; MSWD = 0.46) (Fig. 4b), representing its magma crystallization age.

Zircons from sample XK-8 display short to long prismatic, transparent and colorless. They have lengths of 100–200 μm with length/width ratios from 1:1 to 2:1, weak or oscillatory zoning, and a few have core-rim structure

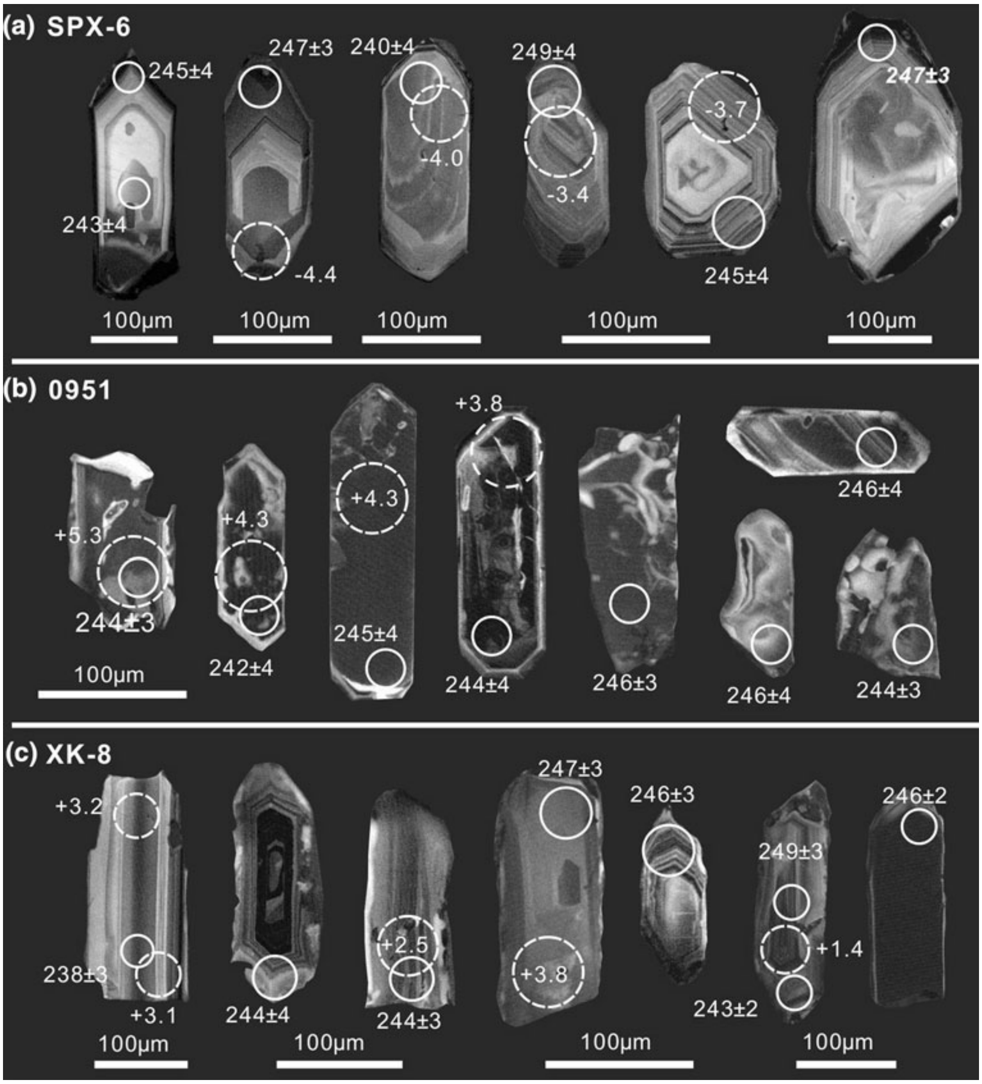

Fig. 3 Representative the CL images of zircon samples. **a** SPX granodiorite (SPX-6); **b** XK granodioritic porphyry (0951); **c** XK granodioritic porphyry (XK-8). The *smaller solid line circles* show LA-ICPMS dating spots and corresponding U–Pb ages (in Ma), and the *bigger broken line circles* show Lu–Hf isotope analysis and corresponding $\varepsilon_{\mathrm{Hf}}(t)$ values

(Fig. 3c). All analyses show U of 207–1,230 ppm, Th of 128–1,499 ppm and Th/U ratios of 0.19–1.22 (Table S2). Five analyses on the inherited cores give $^{206}\mathrm{Pb}/^{238}\mathrm{U}$ ages of 324 ± 4, 264 ± 3, 261 ± 4, 260 ± 4 and 256 ± 3 Ma, respectively (Fig. 4c). The remaining 20 analyses show $^{206}\mathrm{Pb}/^{238}\mathrm{U}$ ages ranging from 234 to 249 Ma, with a weighted mean of 242 ± 2 Ma (2σ; MSWD = 2.9) (Fig. 4c), which is consistent with the age obtained from sample 0951 within error, representing the magma crystallization age of the XK pluton.

Major and trace elements

Major and trace element data for the SPX and XK plutons are given in Table 1. Four samples for the XK diorite from Yang (2008) are also included.

The SPX granodiorite (Table 1 and Fig. 5) is metaluminous and high-K calc-alkaline (Fig. 6a, b). In the trace element spider diagram, all the samples show negative Nb, Ta, Sr, P and Ti anomalies and are relatively enriched in Rb, Ba, Th, U and K (Fig. 7a). Their REE data display strongly fractionated REE patterns ($(\mathrm{La/Yb})_N = 10.1$–$13.7$) and moderately negative Eu anomalies ($\mathrm{Eu/Eu^*} = 0.58$–0.61) (Fig. 7b).

The XK diorites show $\mathrm{SiO_2}$ variation ranging from 52.43 to 56.82 %. Based on the contents of MgO and $\mathrm{Al_2O_3}$ (Fig. 5a–c), they can be divided into two distinct groups: high-Al diorite and high-Mg diorite. The high-Al diorite has $\mathrm{Al_2O_3} = 17.72$–21.11 %, and MgO = 2.50–3.62 % with Mg# of 43–54. The high-Mg diorite is characterized by $\mathrm{Al_2O_3} = 15.32$–16.58 %, and MgO = 5.62–7.62 % with Mg# of 59–64. The contents of CaO,

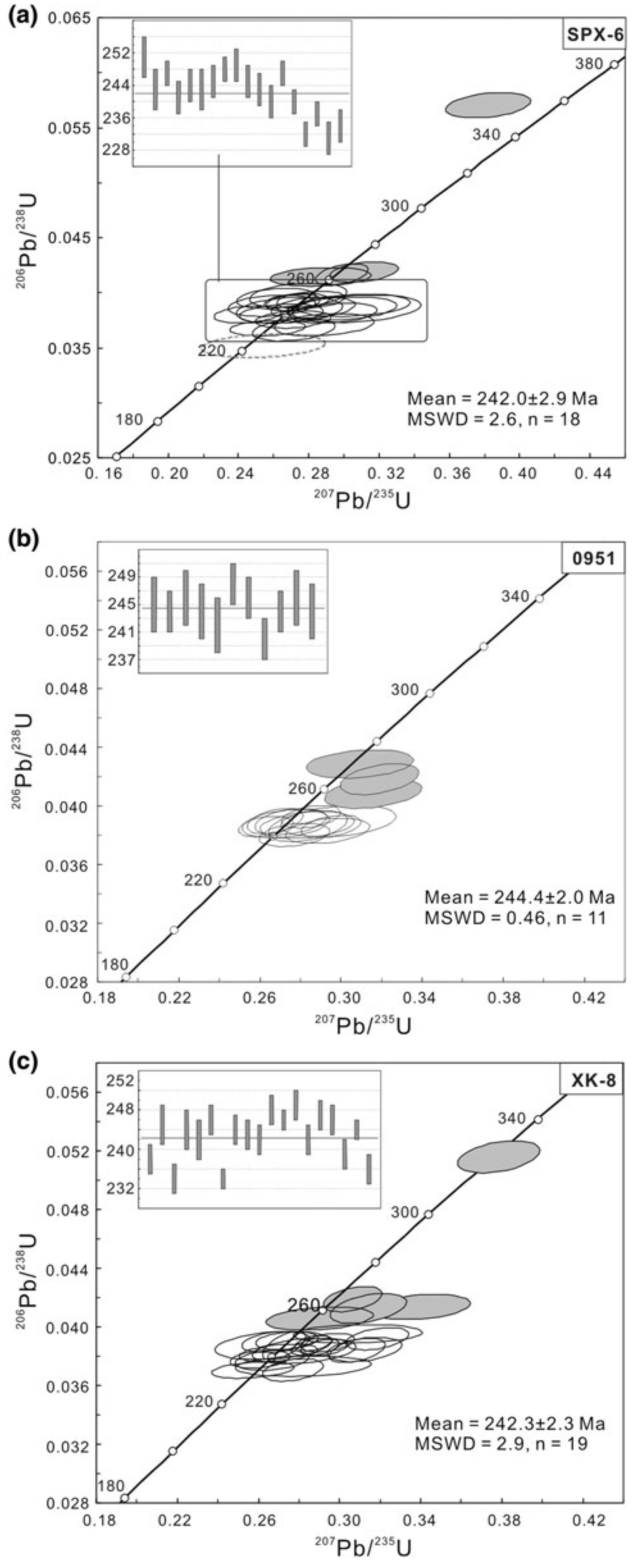

Fig. 4 Zircon U–Pb Concordia diagrams. **a** SPX granodiorite (SPX-6); **b** XK granodioritic porphyry (0951); **c** XK granodioritic porphyry (XK-8). *Shaded* and *dashed ellipses* are not included in the age calculation. *Ellipses* represent 1-sigma uncertainty for individual analyses

Na_2O, TiO_2 and P_2O_5 of the high-Al diorite are relatively higher than those of the high-Mg diorite (Table 1 and Fig. 5). The high-Al diorite straddles the transition between medium-K and high-K calc-alkaline, and the high-Mg diorite falls in the medium-K calc-alkaline field (Fig. 6b). The high-Mg diorite shows high Cr (233–358 ppm) and Ni (51–78 ppm), and relatively low Rb (37.3–57.2 ppm), Sr (305–370 ppm) and Ba (203–297 ppm), whereas the high-Al diorite shows low Cr (21–156 ppm) and Ni (12–40 ppm), and relatively high Rb (38.3–86.9 ppm), Sr (305–725 ppm) and Ba (240–573 ppm) (Fig. 5g–k). All samples from the XK diorites show similar primitive-mantle-normalized trace element patterns with Nb, Ta, P and Ti negative anomalies (Fig. 7a). Their REE data show weakly fractionated REE patterns with $(La/Yb)_N$ ratio of 4.1–6.5 and variable Eu anomalies ($Eu/Eu^* = 0.69$–1.12) (Fig. 7b).

The XK granodioritic porphyry (Table 1 and Fig. 5) is metaluminous (A/CNK = 0.87–0.97) and lies within the medium-K to high-K calc-alkaline fields (Fig. 6). All samples show enrichment of LILE (Rb, Ba, Th, U and K) and depletion of Nb, Ta, P and Ti (Fig. 7a) and display concave-upward REE patterns with weak negative Eu anomalies ($Eu/Eu^* = 0.84$–0.86) (Fig. 7b). The concave-upward REE patterns and weak Eu anomalies in the XK granodioritic porphyry suggest its source containing significant residual amphibole and minor plagioclase.

Isotope geochemistry

Whole-rock Sr and Nd isotopic data are listed in Table 2 and plotted in Fig. 8. For all samples, their initial Sr isotopic ratio (I_{Sr}) and $\varepsilon_{Nd}(t)$ values are calculated at $t = 243$ Ma. The SPX granodiorite shows a narrow variation of I_{Sr} values ranging from 0.7081 to 0.7083 and $\varepsilon_{Nd}(t)$ values ranging from −8.0 to −7.6, with mantle-depleted Nd model ages (T_{DM}) ranging from 1.53 to 1.70 Ga. The XK high-Al diorite has I_{Sr} values of ~0.7060 and $\varepsilon_{Nd}(t)$ values of −1.5 to −1.1, with $T_{DM} = 1.35$–1.40 Ga. The XK high-Mg diorite has I_{Sr} values of 0.7060–0.7063 and $\varepsilon_{Nd}(t)$ values of −2.6 to −2.5, with $T_{DM} = 1.55$–1.63 Ga. The XK granodioritic porphyry has $I_{Sr} = 0.7071$–0.7075, $\varepsilon_{Nd}(t) = -4.5$ and $T_{DM} = 1.30$ Ga.

Zircon Lu–Hf isotopic data are given in Table 3. The initial $\varepsilon_{Hf}(t)$ and T_{DM2} were calculated using their U–Pb zircon ages in Table 3. For sample SPX-6 from the SPX pluton, twelve analyses show $\varepsilon_{Hf}(t)$ values of −4.7 to −3.6 and T_{DM2} of 1.49–1.57 Ga (Fig. 9a, b). For the XK granodioritic porphyry, nine analyses from sample 0951 show $\varepsilon_{Hf}(t)$ values of +3.5 to +5.3 with an average of +4.3 ± 0.5 and T_{DM1} of 0.68–0.76 Ga (Fig. 9a, b). Fourteen analyses from sample XK-8 show $\varepsilon_{Hf}(t)$ values ranging from +0.2 to +5.2, which displays a lager

Table 1 Major (wt. %) and trace element (ppm) data for the SPX and XK Plutons

Sample	0926	0927	SPX-6	0936	0938	0942	P4-05[a]	P7-01[a]	XZ2-01[a]	0946	0948	P2-06[a]	0951	XK-8
Pluton	Shuangpengxi (SPX)			Xiekeng (XK)										
Rock type	Granodiorite			High-Al diorite						High-Mg diorite			Granodioritic porphyry	
SiO_2	63.83	63.85	63.05	55.28	54.31	54.86	56.82	53.23	53.68	55.40	56.00	52.43	62.29	64.72
TiO_2	0.67	0.67	0.69	1.04	1.01	1.06	1.03	1.42	0.93	0.84	0.89	0.85	0.61	0.50
Al_2O_3	15.99	15.93	16.18	21.11	20.81	20.46	17.83	17.72	18.09	15.32	16.58	16.31	17.33	16.92
FeO_t	4.63	4.67	4.92	4.56	4.69	5.35	6.58	7.85	6.12	7.41	6.84	7.61	5.23	2.45
MnO	0.08	0.08	0.09	0.07	0.07	0.08	0.1	0.09	0.06	0.14	0.12	0.14	0.13	0.04
MgO	2.22	2.24	2.52	2.50	3.13	3.03	3.62	3.26	3.36	6.90	5.62	7.62	2.00	1.80
CaO	4.86	4.70	4.95	9.03	9.21	9.14	7.19	9.27	11.07	8.75	8.10	6.94	5.48	4.48
Na_2O	3.03	2.91	2.92	3.68	3.67	3.38	3.06	3.13	2.85	2.68	2.88	3.19	3.40	4.82
K_2O	3.23	3.56	3.28	1.20	1.48	1.26	1.92	1.55	1.92	1.20	1.34	0.92	2.22	3.16
P_2O_5	0.13	0.12	0.15	0.12	0.16	0.08	0.2	0.36	0.19	0.13	0.14	0.13	0.14	0.13
LOI	1.23	1.16	0.69	1.34	1.38	1.18	1.04	1.26	1.03	1.09	1.38	3.11	0.93	0.71
Sum	99.82	99.79	99.61	99.82	99.82	99.79	99.39	99.38	99.34	99.79	99.81	99.45	99.80	99.67
Mg#	46	46	48	49	54	50	50	43	49	62	59	64	41	57
Sc	13.3	13.8	15.2	17.6	18.4	19.9	25.6	19.5	16.9	30.7	27.2	30.4	12.4	7.8
V	95.9	95.3	101	137	158	192	164	96	75.2	186	192	196	83.9	53.9
Cr	30.5	32.3	35.5	59.3	53.8	57.1	156.2	40	20.6	358	244	223.1	20.7	7.03
Co	13.6	13.6	14.7	16.6	17.3	20.5	31.4	20.9	34.6	34.9	31.7	25.4	13.9	9.5
Ni	13.8	13.2	13.6	27.9	25.2	29.4	39.9	18.2	11.8	77.5	74.0	51.2	8.0	2.4
Cu	14.5	17.2	16.5	101	15.3	177	34.2	24.3	149	22.8	38.2	42.3	18.8	12.1
Rb	160	172	149	49.0	38.3	49.6	44.2	86.9	66.6	45.3	57.2	37.3	93.6	81.0
Sr	283	283	298	434	427	408	305	453	725	370	305	315	342	361
Y	28.5	29.2	30.6	22.6	19.4	19.2	23.1	29.3	23.1	20.0	26.4	25.2	23.0	17.3
Zr	194	172	222	112	142	120	112	181	162	62	111	69	178	160
Nb	12.0	11.7	12.3	7.2	4.6	4.5	8.8	9.6	9.9	5.2	7.0	8.2	10.0	8.2
Ba	593	651	654	264	305	240	247	364	573	297	266	203	488	655
Hf	5.33	4.69	5.84	2.93	3.37	3.11	4.27	4.72	5.69	1.82	3.08	2.68	4.49	3.97
Ta	1.00	0.85	0.75	0.51	0.32	0.34	0.54	0.64	0.69	0.35	0.50	0.57	0.74	0.63
Th	17.5	18.4	21.8	3.9	3.1	4.3	3.2	7.8	6.7	3.1	5.7	4.3	10.9	9.1
U	8.09	3.83	2.75	1.01	0.75	1.07	0.78	1.96	1.94	0.91	1.49	1.11	3.31	2.37
La	37.3	42.2	52.1	16.6	11.6	12.9	20.2	30.0	24.3	11.5	17.3	20.3	27.8	24.2
Ce	71.7	81.0	99.4	32.9	24.8	26.4	41.8	62.2	54.8	24.1	36.1	43.6	52.9	46.8
Pr	8.5	9.2	10.9	4.0	3.2	3.3	5.4	7.4	6.7	3.1	4.6	5.6	6.1	5.0
Nd	31.4	34.4	39.5	16.1	13.5	13.4	20.1	29.1	24.8	12.9	18.3	21.9	21.9	17.7
Sm	6.24	6.60	7.22	3.71	3.19	3.10	4.57	5.93	5.03	3.13	4.29	5.00	4.27	3.24
Eu	1.19	1.26	1.30	1.27	1.19	1.18	1.21	1.37	1.85	1.16	1.15	1.27	1.17	0.89
Gd	5.39	5.82	6.27	3.91	3.42	3.32	5.12	6.20	5.10	3.46	4.62	5.50	4.08	3.02
Tb	0.82	0.88	0.92	0.63	0.55	0.54	0.81	0.97	0.78	0.56	0.74	0.93	0.64	0.47
Dy	4.87	5.12	5.47	3.87	3.39	3.30	4.59	5.39	4.41	3.54	4.51	4.99	3.80	2.80
Ho	1.00	1.00	1.08	0.80	0.70	0.69	0.98	1.19	0.95	0.72	0.95	1.10	0.79	0.59
Er	2.72	2.82	2.95	2.25	1.97	1.98	2.56	3.21	2.51	2.08	2.72	2.81	2.27	1.69
Tm	0.40	0.39	0.44	0.33	0.28	0.28	0.42	0.53	0.43	0.31	0.38	0.47	0.33	0.26
Yb	2.66	2.67	2.73	2.20	1.84	1.81	2.81	3.34	2.67	2.00	2.55	2.90	2.37	1.80
Lu	0.40	0.40	0.41	0.32	0.27	0.28	0.40	0.51	0.41	0.30	0.37	0.45	0.37	0.27
$(La/Yb)_N$	10.05	11.31	13.72	5.41	4.53	5.10	5.15	6.43	6.54	4.12	4.87	5.02	8.42	9.61
Eu/Eu*	0.61	0.61	0.58	1.01	1.09	1.12	0.76	0.69	1.11	1.07	0.78	0.74	0.84	0.86

FeO_t = All Fe calculated as FeO; Mg# = (MgO/(MgO + FeO_t)) * 100

[a] Data from Yang (2008)

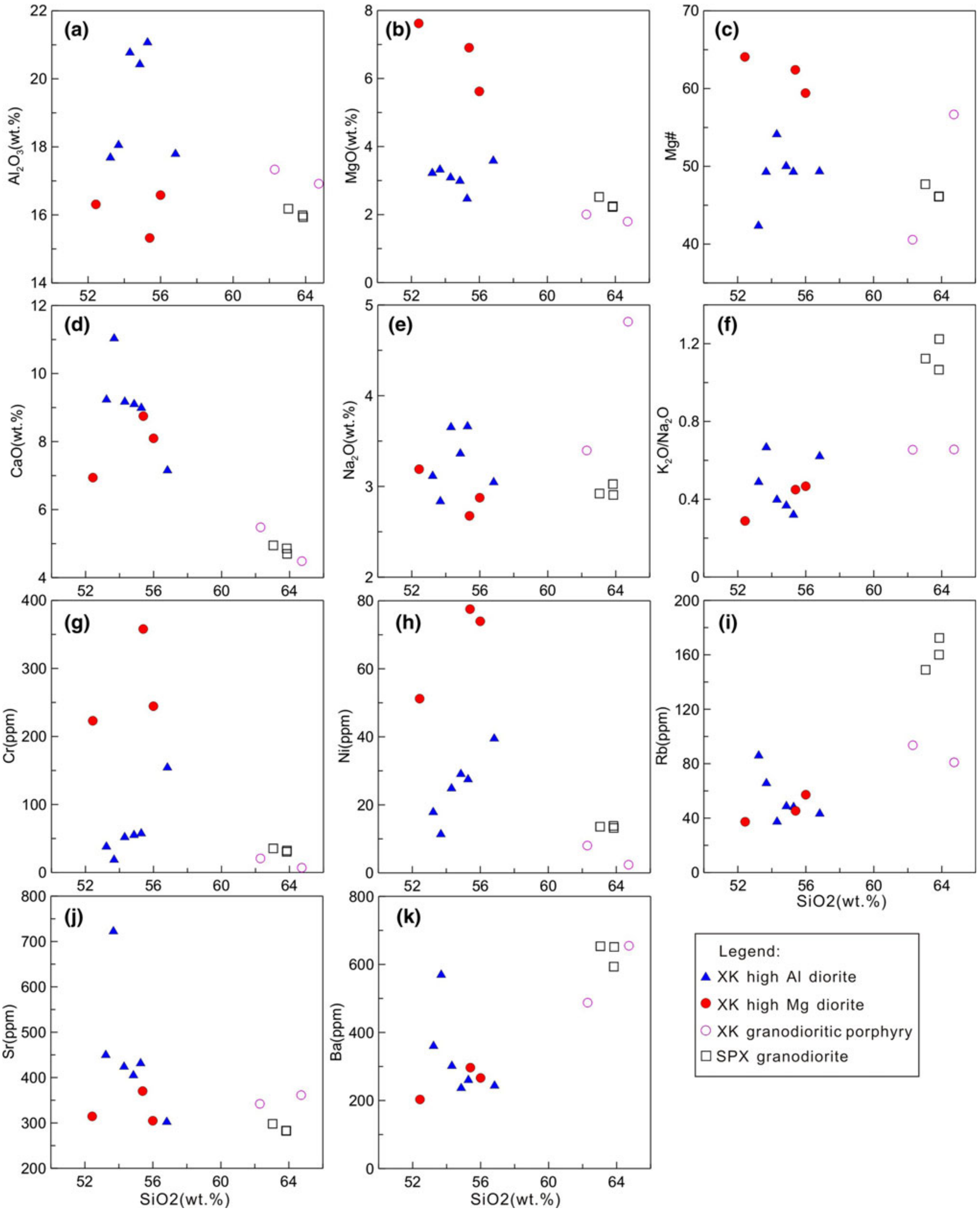

Fig. 5 Harker plots of selected major and trace elements of the SPX and XK plutons. **a** SiO_2 versus Al_2O_3; **b** SiO_2 versus MgO; **c** SiO_2 versus Mg#; **d** SiO_2 versus CaO; **e** SiO_2 versus Na_2O; **f** SiO_2 versus K_2O/Na_2O; **g** SiO_2 versus Cr; **i** SiO_2 versus Ni; **j** SiO_2 versus Sr; **k** SiO_2 versus Ba

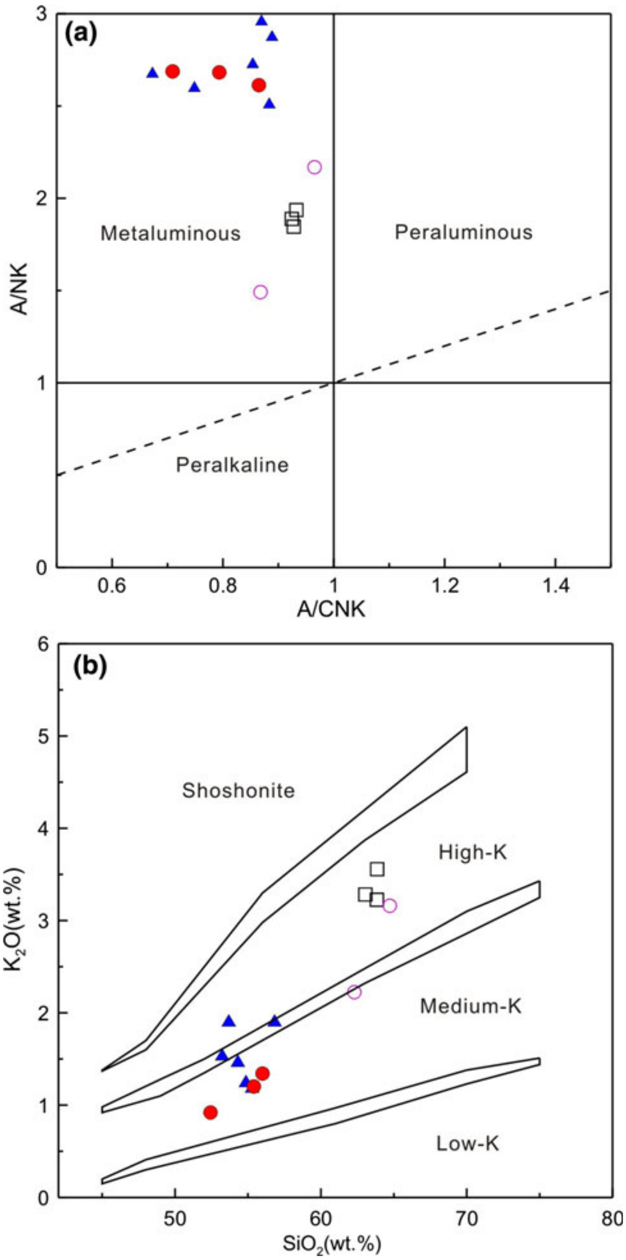

Fig. 6 Plots of **a** A/NK [molar ratio $Al_2O_3/(Na_2O + K_2O)$] versus A/CNK molar ratio [$Al_2O_3/(CaO + Na_2O + K_2O)$] and **b** SiO_2 versus K_2O (Peccerillo and Taylor 1976). Symbols as in Fig. 5

variation than the sample 0951(Fig. 9a). The single-stage model ages range from 0.68 to 0.89 Ga (Fig. 9b).

Discussion

Petrogenesis

Shuangpengxi granodiorite

The SPX granodiorite has I_{Sr} (~0.708), negative $\varepsilon_{Nd}(t)$ (~−8.0) and negative $\varepsilon_{Hf}(t)$ (~−4.2), coupled with Nd and Hf model ages of ~1.5–1.7 Ga, suggesting that its magma was predominantly derived from Meso-Paleoproterozoic crustal materials. As shown in Fig. 8, the granodiorite overlaps with the field of the West Qinling crust-derived granitoids (Zhang et al. 2007a), interpreted to have originated from partial melting of high-K basaltic protoliths in the lower crust.

Experiments of studies have demonstrated that partial melting of mafic rocks can generate melts of metaluminous granitic composition (Rushmer 1991; Wolf and Wyllie 1994). Moyen and Stevens (2006) have compiled nearly all experimental data about the partial melting of amphibolites, showing that melts formed by partial melting of low-K mafic rocks usually have low K_2O and $Na_2O/K_2O >1$. Medium- to high-K calc-alkaline granitic magmas can be derived from partial melting of hydrous calc-alkaline to high-K calc-alkaline, mafic to intermediate metamorphic rocks (Roberts and Clemens 1993; Sisson et al. 2005). The melting reactions would result from fluid-absent breakdown of biotite and hornblende, leaving a plagioclase-enriched and amphibole-poor residue (Sisson et al. 2005). The SPX granodiorite is metaluminous and has high K_2O with $Na_2O/K_2O <1$, indicating that a medium- to high-K basaltic protolith was required. Strongly fractionated REE patterns and moderate negative Eu anomalies (Table 1) of the granodiorite suggest magma generation by amphibole dehydration reaction with plagioclase-enriched residue. All these characteristics support a derivation of the SPX granodiorite from partial melting of medium- to high-K basaltic protolith.

Xiekeng diorites

The XK diorites contain two distinct groups: high-Mg diorite and high-Al diorite. The high-Mg diorite has high MgO (5.62–7.62 %), Mg# (59–64), Cr (233–358 ppm) and Ni (51–78 ppm), indicating that its magma was dominantly mantle-derived. The high-Al diorite has relatively low Mg#, Cr and Ni (Table 1), but its Mg# is still higher than the experimental melts produced by melting of metabasalts and eclogites (usually, Mg# <45) (Rapp and Watson 1995; Rapp et al. 1999), implying that its magma was also mantle-derived. The XK diorites (including high-Mg diorite and high-Al diorite) have $I_{Sr} = \sim 0.706$ and $\varepsilon_{Nd}(t) = \sim -3$ to -1 (Table 2 and Fig. 8), suggesting that their magma could be derived from enriched lithospheric mantle.

At convergent margins, Sisson and Grove (1993) defined high-alumina basalts (HABs) with $SiO_2 \leq 52$ % (some <54 %) and high-alumina basaltic andesites (HABAs) with $SiO_2 \leq 57$ %. Both HABAs and HABs have $Al_2O_3 >17$ %, with a typical range from 18.5 to 20.5 %. Most HABs and HABAs have low MgO (<6 % and <5 %, respectively) and low Mg# (40–50). The chemical

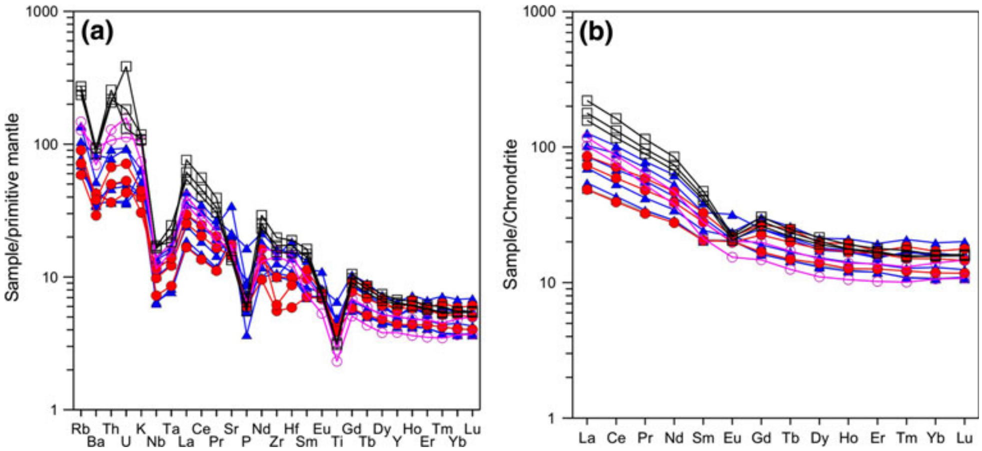

Fig. 7 Primitive-mantle (PM)-normalized trace element spider diagrams and chondrite-normalized REE patterns. Chondrite and PM values are from Sun and McDonough (1989). *Symbols* as in Fig. 5

Table 2 Data for whole-rock Sr and Nd isotopes

Sample	^{87}Rb/^{86}Sr	^{87}Sr/^{86}Sr	±2σ	$(^{87}Sr/^{86}Sr)_0$	^{147}Sm/^{144}Nd	^{143}Nd/^{144}Nd	±2σ	$\varepsilon_{Nd}(t)$	T_{DM}(Ga)
SPX granodiorite									
0926	1.640	0.713920	6	0.7083	0.120	0.512106	3	−8.0	1.70
0927	1.769	0.714222	5	0.7081	0.116	0.512104	2	−7.9	1.63
0927R	1.769	0.714249	5	0.7081	0.116	0.512112	2	−7.8	1.62
SPX-6	1.450	0.713340	4	0.7083	0.111	0.512112	8	−7.6	1.53
XK diorites									
0936	0.327	0.707156	5	0.7060	0.140	0.512469	2	−1.5	1.40
0942	0.353	0.707177	4	0.7060	0.139	0.512491	2	−1.1	1.35
0946	0.355	0.707557	4	0.7063	0.147	0.512431	2	−2.5	1.63
0948	0.544	0.707893	6	0.7060	0.142	0.512417	2	−2.6	1.55
XK granodioritic porphyry									
0951	0.793	0.709829	6	0.7071					
XK-8	0.650	0.709786	4	0.7075	0.111	0.512273	9	−4.5	1.30

^{87}Rb/^{86}Sr and ^{147}Sm/^{144}Nd ratios are calculated using Rb, Sr, Sm and Nd contents (Table 1), measured by ICP-MS; $\varepsilon_{Nd}(t)$ values are calculated using present-day $(^{147}Sm/^{144}Nd)_{CHUR} = 0.1967$ and $(^{143}Nd/^{144}Nd)_{CHUR} = 0.512638$; T_{DM} values are calculated using present-day $(^{147}Sm/^{144}Nd)_{DM} = 0.2137$ and $(^{143}Nd/^{144}Nd)_{DM} = 0.51315$

composition of the XK high-Al diorite (Table 1) is very similar to that of the HABAs, suggesting that they share a similar petrogenesis.

Two types of petrogenetic models have been proposed for the origin of low-MgO HABs and HABAs: (1) derivative melts produced by fractional crystallization of a primitive-mantle-derived magma (Sisson and Grove 1993) and (2) derivative melts that had undergone preferential accumulation of plagioclase (Crawford et al. 1987; Wagner et al. 1995). The above two models suggest that the low-MgO HABs and HABAs are not primitive-mantle-derived magma and that H_2O plays an important role in their magma evolution. The main effects of H_2O on crystallization of mafic melts are to decrease melt temperature and to suppress plagioclase crystallization relative to olivine and clinopyroxene (Danyushevsky 2001). Fractionation of some Al-poor mafic phases such as olivine and pyroxene will reduce the contents of MgO, Cr and Ni, but increase the contents of Al_2O_3 and other incompatible elements in the residual melts.

The XK high-Al diorite contains some hydrous minerals such as hornblende and biotite (Fig. 2a), indicating that its parental magma carried some extent of water. Both clinopyroxene and orthopyroxene are locally enclosed in plagioclase (Fig. 2a), indicative of early crystallization. The XK high-Al diorite displays low MgO, Cr and Ni, and high Al_2O_3, Rb, Sr and Ba, probably due to the fractionation of olivine and pyroxene. Sisson and Grove (1993) pointed out that low-MgO HABs and HABAs with Al_2O_3 >20 % are rare and those with >21 % Al_2O_3 are very uncommon. Some samples of the XK high-Al_2O_3 diorite contain Al_2O_3 up to 21.11 %, implying plagioclase accumulation, consistent with abundant plagioclase (60–75 %) in these samples (Fig. 2a). The XK high-Al diorite shows obvious

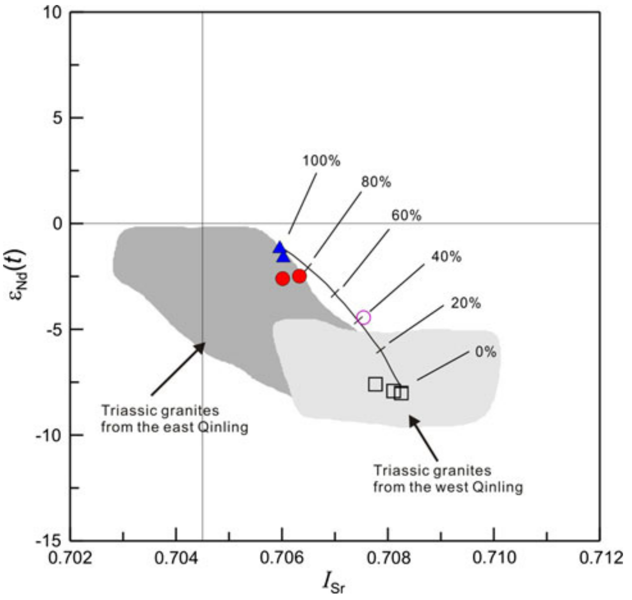

Fig. 8 I_{Sr} versus $\varepsilon_{Nd}(t)$ plot for the SPX and XK plutons. *Symbols* as in Fig. 5. Triassic granites of the West Qinling from Zhang et al. (2007a); Triassic granites of the east Qinling from Zhang et al. (2007a), Qin et al. (2010b), Jiang et al. (2010). $\varepsilon_{Nd}(t)$ and I_{Sr} values are calculated at $t = 243$ Ma. The parameters used in the modeling are as follows: Mantle-derived end-member: Sr = 305 ppm, Nd = 20 ppm, $I_{Sr} = 0.7060$, $\varepsilon_{Nd}(t) = -1.1$; Crustal-derived end-member: Sr = 370 ppm, Nd = 15 ppm, $I_{Sr} = 0.7083$, $\varepsilon_{Nd}(t) = -7.9$

positive correlations between Eu/Eu* ratios and the contents of CaO and Sr (Fig. 10a, b), together with positive Eu anomalies (Eu/Eu* = 1.1–1.2) further supporting accumulation of plagioclase. Thus, we suggest that the XK high-Al diorite was not directly solidified from a primitive-mantle-derived magma, but it had experienced fractional crystallization of olivine and pyroxene and/or preferential accumulation of plagioclase.

The XK high-Mg diorite is similar to the high-Mg andesites (HMAs) in the Setouchi Volcanic Belt in MgO (Mg#), Cr and Ni (Tatsumi 2006 and references therein). However, high-Mg diorites should not simply interpreted to be the solidification of the HMA magma, because the high-Mg diorites may be the cumulate of some mafic magma (Kamei et al. 2004). The XK high-Mg diorite has relatively less MgO, Mg# and Ni (Table 1) than the primary arc basalts (usually MgO of 8–10 %, Mg# of 63–71 and Ni of 85–245 ppm) (Kelemen et al. 2003), suggesting olivine fractionation. The high Cr (233–358 ppm) for the XK high-Mg diorite suggests accumulation of pyroxene, which is also in good agreement with our petrographic observation that the pyroxene volume of the high-Mg diorite (sample 0946) is more abundant than that of the high-Al diorite (sample 0942) (Fig. 2a, b). For the high-Mg diorite, positive correlations between Eu/Eu* ratios and the contents of CaO and Sr (Fig. 10a, b) indicate plagioclase accumulation. Thus, we suggest that the XK high-Mg diorite was not directly solidified from the HMA magma, but was derived from fractional crystallization of olivine and/or preferential accumulation of pyroxene of a hydrous basaltic magma.

The I_{Sr} of the XK high-Al diorite and the high-Mg diorite is uniform over a wide range of Mg#, and $\varepsilon_{Nd}(t)$ shows a small variation (Fig. 10c, d), suggesting that the two diorites are consanguineous, but have undergone different magmatic differentiation processes. Both of them have subduction-related geochemical signatures, characterized by enrichment of LILE (Rb, Ba and K) and LREE and depletion of HFSE (Nb, Ta and Ti) (Fig. 7a, b), suggesting that their mantle source was modified by slab-derived fluid or melt. We use some trace element ratios to assess the modification of slab-derived components.

Large-ion lithophile elements (e.g., Rb, Ba, Sr, K and U) are effectively transported by the fluid phases, but thorium, LREE and HFSE could be mobilized mainly by melts (Pearce and Peate 1995; Elliott et al. 1997; Class et al. 2000). Mafic magma showing high Ba/La and Ba/Th is commonly interpreted to reflect the addition of an aqueous fluid from the slab (Pearce and Peate 1995; Elliott et al. 1997), whereas high Th/Nb and Th/Yb ratios in mafic magma are ascribed to modifications by slab melts (Johnson and Plank 1999; Class et al. 2000). The XK diorites have high Th/Yb ratios (1.12–2.49) and Th/Nb ratios (0.36–0.94) and relatively low Ba/La ratios (10.0–26.3) and Ba/Th ratios (46.6–98.7) (Fig. 10e, f), suggesting the significant involvement of sediment-derived melt in their mantle source, as consistent with $I_{Sr} = \sim 0.706$ and $\varepsilon_{Nd}(t) = \sim -3$ to -1 (Fig. 8) (e.g., Hawkesworth et al. 1997; Dokuz 2011).

Xiekeng granodioritic porphyry

The XK granodioritic porphyry has similar SiO_2 as the SPX granodiorite (Table 1), but distinct Sr, Nd and Hf isotopic compositions (Fig. 8 and Fig. 9). The XK granodioritic porphyry is closely associated with the XK diorites, suggesting that there is a genetic link between them. Two possible processes can explain the generation of the XK granodioritic porphyry: (1) crustal assimilation and fractional crystallization (AFC) of the diorite magma and (2) mixing between mantle-derived and crust-derived magmas.

The potential crustal assimilation components could be Devonian to Triassic sediments in the West Qinling. According to Sm–Nd isotopic data from Chen et al. (2008), the calculated ε_{Nd}(243 Ma) values for those sediments range from −8.3 to −16.3, lower than the values (−4.5) of the XK granodioritic porphyry. This indicates that assimilation of sediments in the magma was rather limited. Alternatively, we propose that the XK granodioritic porphyry was produced by mixing of mantle-derived melt with crustal melt. A simple two end-members mixing model was tested using

Table 3 Zircon Lu–Hf isotopic data

Analysis	^{176}Yb/^{177}Hf	^{176}Lu/^{177}Hf	^{176}Hf/^{177}Hf	±(1 s)	Age (Ma)	$\varepsilon_{\mathrm{Hf}}(t)$	±(1 s)	T_{DM1} (Ma)	±(1 s)	T_{DM2} (Ma)	±(1 s)
SPX granodiorite											
SPX-6-01	0.013995	0.000715	0.282519	0.000006	244	−3.7	0.2	1,030	18	1,505	28
SPX-6-02	0.012692	0.000659	0.282520	0.000008	244	−3.6	0.3	1,027	22	1,501	35
SPX-6-03	0.022675	0.001114	0.282529	0.000011	244	−3.4	0.4	1,026	31	1,485	49
SPX-6-04	0.013940	0.000697	0.282503	0.000008	244	−4.3	0.3	1,052	22	1,540	36
SPX-6-05	0.012608	0.000638	0.282498	0.000007	244	−4.4	0.3	1,057	20	1,551	32
SPX-6-06	0.017363	0.000876	0.282506	0.000006	244	−4.2	0.2	1,052	18	1,534	29
SPX-6-07	0.016163	0.000838	0.282497	0.000006	244	−4.5	0.2	1,064	17	1,555	28
SPX-6-08	0.016869	0.000869	0.282501	0.000007	244	−4.4	0.2	1,060	19	1,546	30
SPX-6-09	0.012866	0.000656	0.282511	0.000009	244	−4.0	0.3	1,040	24	1,522	38
SPX-6-10	0.011007	0.000580	0.282490	0.000009	244	−4.7	0.3	1,067	24	1,568	39
SPX-6-11	0.014918	0.000780	0.282491	0.000007	244	−4.7	0.3	1,071	20	1,568	33
SPX-6-12	0.017582	0.000916	0.282511	0.000008	244	−4.0	0.3	1,047	24	1,525	38
XK granodioritic porphyry											
0951-01	0.017734	0.000905	0.282746	0.000008	244	4.3	0.3	716	22	998	36
0951-02	0.037103	0.001790	0.282780	0.000008	244	5.3	0.3	684	23	930	35
0951-03	0.025235	0.001260	0.282748	0.000008	244	4.3	0.3	720	23	996	37
0951-04	0.027882	0.001288	0.282751	0.000011	244	4.4	0.4	716	31	989	50
0951-05	0.027805	0.001381	0.282724	0.000012	244	3.5	0.4	756	33	1,050	52
0951-06	0.022851	0.001254	0.282728	0.000013	244	3.6	0.4	748	36	1,041	56
0951-07	0.030574	0.001522	0.282729	0.000014	244	3.6	0.5	753	40	1,043	63
0951-08	0.024656	0.001258	0.282752	0.000009	244	4.5	0.3	714	25	986	39
0951-09	0.019695	0.001010	0.282732	0.000013	244	3.8	0.4	738	35	1,030	56
XK granodioritic porphyry											
XK-8-01	0.030557	0.001562	0.282717	0.000010	244	3.2	0.4	771	29	1,069	45
XK-8-02	0.025946	0.001451	0.282632	0.000010	244	0.2	0.4	889	29	1,259	45
XK-8-03	0.023269	0.001274	0.282682	0.000009	244	2.0	0.3	815	26	1,146	41
XK-8-04	0.023100	0.001247	0.282658	0.000009	244	1.1	0.3	848	25	1,199	40
XK-8-05	0.021452	0.001125	0.282664	0.000008	244	1.4	0.3	836	23	1,184	37
XK-8-06	0.017701	0.000904	0.282770	0.000008	244	5.2	0.3	681	23	942	37
XK-8-07	0.014640	0.000877	0.282753	0.000009	244	4.5	0.3	706	24	981	39
XK-8-08	0.016512	0.000797	0.282731	0.000007	244	3.8	0.3	735	21	1,029	33
XK-8-09	0.011644	0.000702	0.282758	0.000008	244	4.8	0.3	695	24	967	38
XK-8-10	0.013821	0.000735	0.282701	0.000008	244	2.7	0.3	776	21	1,096	34
XK-8-11	0.018220	0.000609	0.282731	0.000005	244	3.8	0.2	731	14	1,028	23
XK-8-12	0.033902	0.001277	0.282667	0.000009	244	1.4	0.3	836	27	1,179	42
XK-8-13	0.050824	0.001611	0.282700	0.000006	244	2.5	0.2	796	19	1,108	29
XK-8-14	0.037184	0.001251	0.282713	0.000006	244	3.1	0.2	769	16	1,074	25

The single-stage Hf model age (T_{DM1}) is taken for positive $\varepsilon_{\mathrm{Hf}}(t)$, and two-stage Hf model age (T_{DM2}) is taken for negative $\varepsilon_{\mathrm{Hf}}(t)$ (Zheng et al. 2006)

Sr–Nd isotopic data. In this modeling, the XK diorite represents the mantle-derived magma end-member and the SPX granodiorite represents the crustal end-member. Sample XK-8 from the XK granodioritic porphyry plots on the mixing curve, showing that the XK granodioritic porphyry could contain ~40 % mantle-derived component (Fig. 8).

Zircon Hf isotopic data provide additional evidence for the magma mixing. Zircons in the sample 0951 have a homogeneous Hf isotopic composition, with average $\varepsilon_{\mathrm{Hf}}(t) = 4.3 \pm 0.5$. Zircons in the sample XK-8 have $\varepsilon_{\mathrm{Hf}}(t) = +0.2$ to $+5.2$, which shows a larger variation (with ~5 $\varepsilon_{\mathrm{Hf}}(t)$ units) than the sample 0951 (Fig. 9a). Such variation can only be reconciled by the operation of open-system processes or reflect the hybrid melt at the time of crystallization (Kemp et al. 2007; Yang et al. 2007).

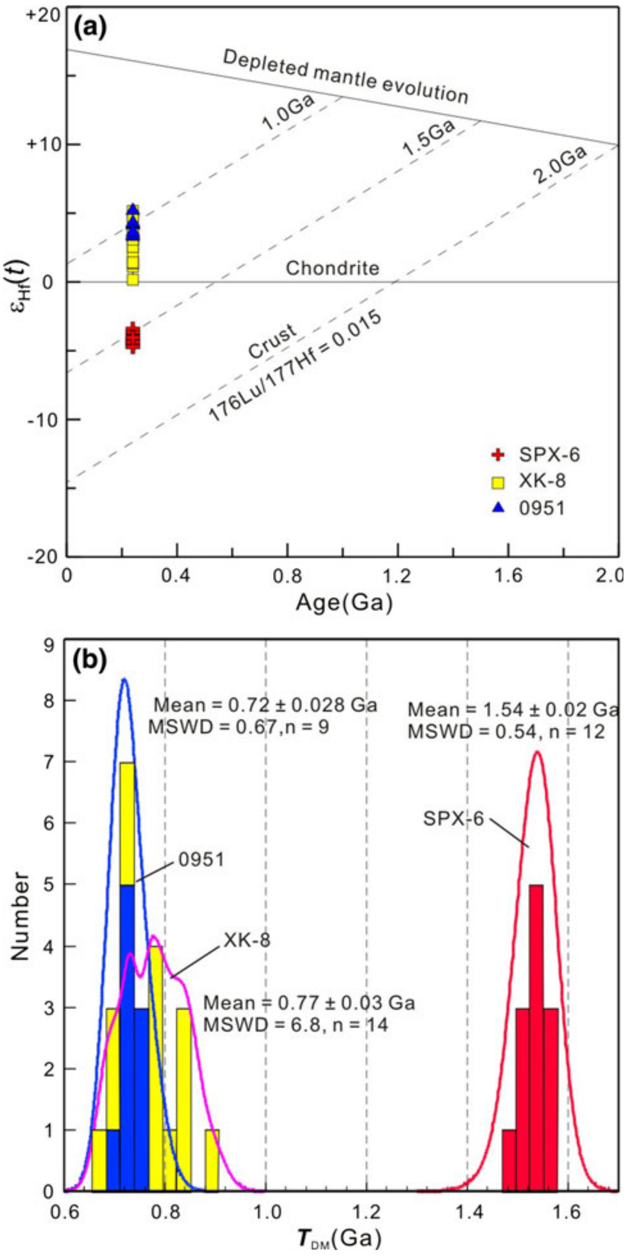

Fig. 9 Zircon Hf isotopic compositions of the SPX granodiorite and XK granodioritic porphyry. **a** $^{206}Pb/^{238}U$ age-$\varepsilon_{Hf}(t)$ variations and **b** Histograms of zircon T_{DM} values for the SPX and XK plutons. The single-stage Hf model age (T_{DM1}) is taken for positive $\varepsilon_{Hf}(t)$, and two-stage Hf model age (T_{DM2}) is taken for negative $\varepsilon_{Hf}(t)$ (Zheng et al. 2006)

Tectonic implications

The Early Indosinian tectonic setting in the West Qinling is still controversial. Some researchers explain the Early Indosinian granitoids in the West Qinling to be subduction-related (Jin et al. 2005; Meng et al. 2005). However, other studies advocate that they formed in an early stage after collision (Zhang et al. 2006, 2008). The debate focuses mainly on the timing of final closure of the A'nimaque-Mianlue oceans. In the middle part of the West Qinling, two quartz diorite plutons (Yeliguan and Xiahe) have been dated at 245 ± 6 and 238 ± 4 Ma (Fig. 1b), respectively, and interpreted to have formed in the active plate margin (Jin et al. 2005). Meng et al. (2005) have synthesized the Triassic sedimentary stratigraphy in the East and West Qinling, pointing out that Lower Triassic-Anisian sequences in the East Qinling are composed exclusively of shallow-marine facies, with an angular unconformity above the early Anisian (245–237 Ma) sequence. However, in the middle part of the West Qinling, the shallow-marine facies did not disappear until the early Ladinian (237–228 Ma), and terrestrial facies were dominant in the Late Triassic (Yin et al. 1992; Meng et al. 2005). Therefore, Meng et al. (2005) proposed that the Mianlue Ocean in the East Qinling had been closed during the Middle Triassic due to the South China block's clockwise rotation and diachronous collision with the North China block, while the A'nimaque Ocean in the West Qinling was still in the process of subduction and formation of the magmatic arc.

There are many lines of evidence arguing that the West Qinling was not an active margin in the Early Indosinian. Metamorphic ages of 242–221 Ma of the Mianlue ophiolite suggest the Mianlue Ocean had been closed at least in the Early Triassic (Li et al. 1996). The regional angular unconformity in the East Kunlun between the Late Permian Gequ Formation and underlying Middle Permian Shuweimenke Formation represents the closure of the A'nimaque Ocean and continental collision (Yin and Zhang 1998; Ren 2004; Chen et al. 2010). The Late Gequ Formation, a typical molasse formation, consists of a basal conglomerate with a Changxinggian biostratigraphic age (254–251 Ma) and also unconformably overlies ophiolitic mélange within the A'nimaque suture zone (Ren 2004; Chen et al. 2010). Sedimentologically, an abrupt change of facies occurred in the northwestern part of the West Qinling during the middle Triassic (Meng et al. 2005). However, the cessation of marine deposition cannot necessarily mark the continental collision, because marine deposition may continue in the residual sea after the collision, like for the Cenozoic India-Asia collision (e.g., Wu et al. 2008). As documented by this and previous studies (Feng et al. 2002; Jin et al. 2005; Zhang et al. 2006; Wang et al. 2010), the widespread magmatism in the middle and western parts of the West Qinling occurred in the Early Indosinian with an age-span of ~245–235 Ma (Fig. 1b), which post-dates Late Permian closure of the A'nimaque Ocean. We suggest that the A'nimaque Ocean had disappeared at the end of the Middle Permian and the Early Indosinian magmatism in the West Qinling formed in an early stage after collision.

For post-collisional granitoids, many studies proposed that slab break-off or lithosphere delamination can account

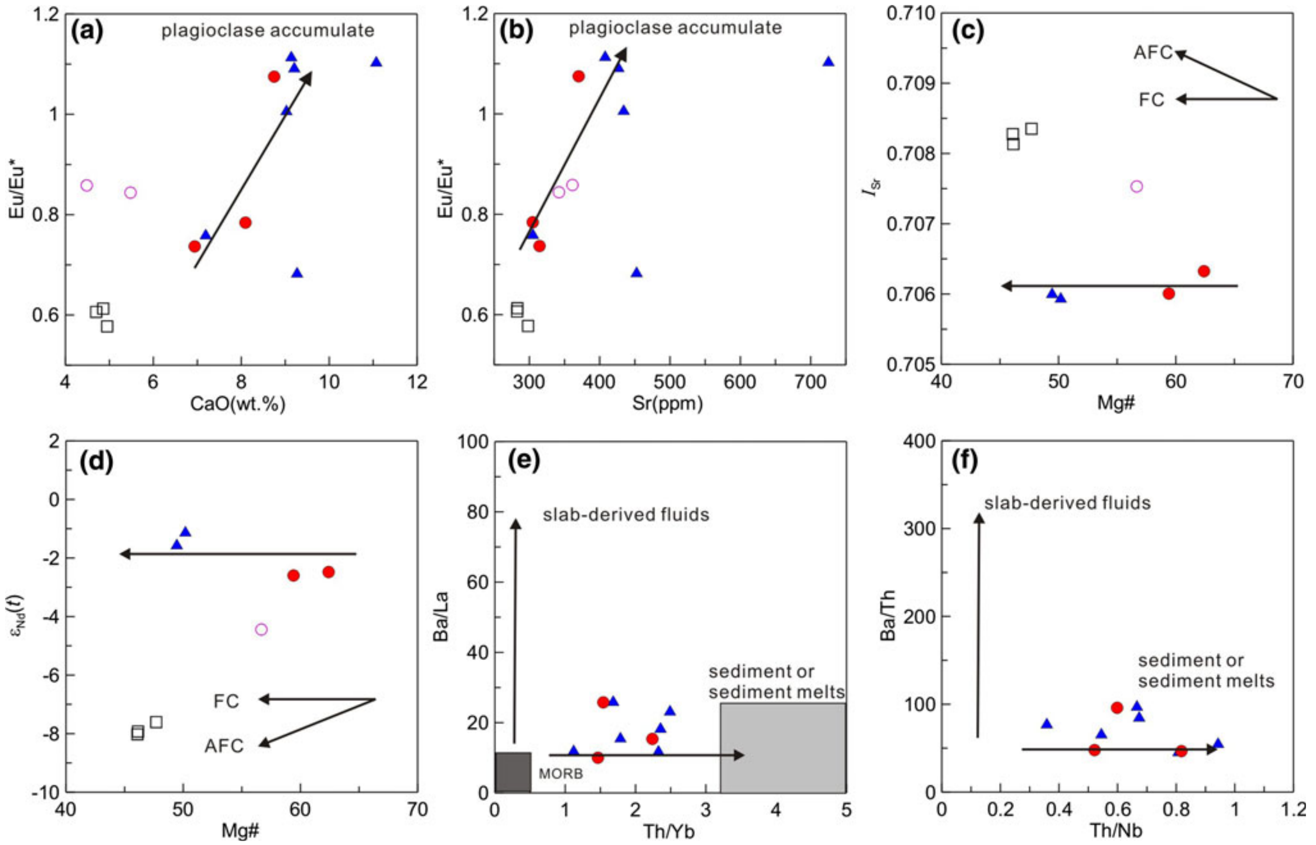

Fig. 10 **a** CaO versus Eu/Eu* diagram; **b** Sr versus Eu/Eu* diagram; **c** Mg# versus I_{Sr} diagram; **d** Mg# versus $\varepsilon_{Nd}(t)$ diagram; **e** Th/Yb versus Ba/La diagram (after Dokuz 2011); and **f** Th/Nb versus Ba/Th diagram (after Elliott et al. 1997). *Symbols* as in Fig. 5. *FC* fractional crystallization, *AFC* assimilation fractional crystallization

for their magma generation (e.g., Davies and von Blanckenburg 1995; Wortel and Spakman 2000; Atherton and Ghani 2002; Bonin 2004; Massonne 2005; Altunkaynak 2007; Mahéo et al. 2009; Dokuz 2011). Lithospheric delamination may result from gravitational instability due to lithospheric thickening, and cause asthenosphere upwelling, that can induce partial melting of the remaining lithospheric mantle. Alternatively, the break-off of a subducted oceanic slab will create a gap, which is rapidly filled with the upwelling mantle asthenosphere, triggering partial melting of the overlying lithosphere. Generally, magmatism caused by the lithospheric delamination shows a regional distribution (Mahéo et al. 2009 and references therein), whereas magmatism resulted from slab break-off shows a linear distribution with rapidly crustal uplift parallel to the suture zone (Rogers et al. 2002; Buiter et al. 2002; Gerya et al. 2004; Mahéo et al. 2009; Duretz et al. 2011). The NW–SE linear distribution of the Early Indosinian intrusive rocks in the West Qinling (Fig. 1b) suggests that slab break-off is a possible mechanism for the Early Indosinian magma generation in the West Qinling.

Based on numerical modeling (Davies and von Blanckenburg 1995; Van de Zedde and Wortel 2001; Li et al. 2002; Duretz et al. 2011), slab break-off occurs at 40–300 km depth starting 4–19 M.yr after continental lithosphere subduction. The Early Indosinian magmatism in the West Qinling took place at ~245 Ma, ~9 M.yr after the onset (~254 Ma) of continental subduction (Wang et al. 1997; Chen et al. 2010). This is consistent with the timescale for slab break-off. The abrupt change from Middle Triassic marine facies to Upper Triassic terrestrial facies and the absence of the upper part of Middle Triassic (Ladinian) sequences in the northwestern part of the West Qinling (Yin et al. 1992; Meng et al. 2005) may reflect rapid crustal uplift due to slab break-off (Buiter et al. 2002; Rogers et al. 2002; Gerya et al. 2004). Furthermore, K-feldspar $^{40}Ar/^{39}Ar$ multiple diffusion domain (MDD) modeling, combined with the biotite $^{40}Ar/^{39}Ar$ age from the pluton in the east of Xiahe, reveals a rapid cooling history (17.75 °C/Ma) from 240 to 230 Ma, implying a fast uplift (Zheng et al. 2004), responding to the influx of mantle asthenosphere following slab break-off.

Conclusions

U–Pb zircon dating indicates that the SPX and the XK plutons were formed contemporaneously at ~244 Ma. The Early Indosinian magmatism in the West Qinling fits well to the model of Deep Crustal Hot Zones (Annen et al. 2006, 2008). The XK diorites were derived from partial melting of enriched lithospheric mantle that had been modified by slab-derived melt. The hydrous basaltic magmas were successively emplaced in the lower crust, providing the necessary heat source and volatiles to induce the partial melting of the lower crust. The XK high-Al diorite was formed by the hydrous basaltic magmas that had experienced fractional crystallization of olivine and pyroxene and/or preferential accumulation of plagioclase, while the XK high-Mg diorite was formed by fractional crystallization of olivine and/or preferential accumulation of pyroxene. The SPX granodiorite originated from dehydration melting of lower crust due to heat input from mantle magma. The XK granodioritic porphyry was generated by mixing of residual mantle-derived melt and crustal melt. Combined with regional studies, we interpret this Early Indosinian magmatism in the West Qinling to result from break-off of the subducted A'nimaque oceanic slab soon after collision. The slab break-off model can explain the linear distribution of the Early Indosinian plutons and rapid crustal uplift during the Middle Triassic in the West Qinling orogen.

Acknowledgments This research was supported by SinoProbe 04-02 (No. 2101105), China Geological Survey (No. 1212011220276) and the Autonomous Subject of GPMR, Wuhan (No. 124-G08 Y60104). F. Corfu and two anonymous reviewers are thanked for their thoughtful reviews, which greatly helped us to improve the paper. Authors also thank Dr. Yong-Sheng Liu for LA-ICP-MS zircon U–Pb dating and Dr. Zhao-Chu Hu for LA-MC-ICM-MS Zircon Hf isotopic analyses and Dr. Yuan-Bao Wu for his helpful discussion.

References

Altherr R, Henjes-Kunst F, Langer C, Otto J (1999) Interaction between crustal-derived felsic and mantle-derived mafic magmas in the Oberkirch Pluton (European Variscides, Schwarzwald, Germany). Contrib Mineral Petrol 137(4):304–322

Altunkaynak S (2007) Collision-driven slab breakoff magmatism in northwestern Anatolia, Turkey. J Geol 115(1):63–82

Andersen T (2002) Correction of common lead in U–Pb analyses that do not report 204Pb. Chem Geol 192(1–2):59–79

Annen C, Sparks R (2002) Effects of repetitive emplacement of basaltic intrusions on thermal evolution and melt generation in the crust. Earth Planet Sci Lett 203(3–4):937–955

Annen C, Blundy JD, Sparks R (2006) The genesis of intermediate and silicic magmas in deep crustal hot zones. J Petrol 47(3):505

Annen C, Blundy JD, Sparks RSJ (2008) The sources of granitic melt in Deep Hot Zones. Trans R Soc Edinb Earth Sci 97(04):297–309

Atherton MP, Ghani AA (2002) Slab breakoff: a model for Caledonian, Late Granite syn-collisional magmatism in the orthotectonic (metamorphic) zone of Scotland and Donegal, Ireland. Lithos 62(3–4):65–85

Barbarin B (2005) Mafic magmatic enclaves and mafic rocks associated with some granitoids of the central Sierra Nevada batholith, California: nature, origin, and relations with the hosts. Lithos 80(1–4):155–177

Bergantz GW (1989) Underplating and partial melting: implications for melt generation and extraction. Science 245(4922):1093–1095

Blichert-Toft J (2008) The Hf isotopic composition of zircon reference material 91500. Chem Geol 253(3–4):252–257

Blichert-Toft J, Chauvel C, Albarède F (1997) Separation of Hf and Lu for high-precision isotope analysis of rock samples by magnetic sector-multiple collector ICP-MS. Contrib Mineral Petrol 127(3):248–260

Bonin B (2004) Do coeval mafic and felsic magmas in post-collisional to within-plate regimes necessarily imply two contrasting, mantle and crustal, sources? A review. Lithos 78(1–2):1–24

Buiter SJH, Govers R, Wortel M (2002) Two-dimensional simulations of surface deformation caused by slab detachment. Tectonophysics 354(3–4):195–210

Cao XF, Lü XB, Yao SZ, Mei W, Zou XY, Chen C, Liu ST, Zhang P, Su YY, Zhang B (2011) LA-ICP-MS U–Pb zircon geochronology, geochemistry and kinetics of the Wenquan ore-bearing granites from West Qinling, China. Ore Geol Rev 43(1):120–131

Chen YL, Li DP, Zhou J, Zhang HF, Liu F, Nie LS, Jiang LT, Liu XM (2008) U–Pb ages of zircons in western Qinling Shan, China, and their tectonic implications. Earth Sci Front 15(4):88–107

Chen SJ, Li RS, Ji WH, Zhao ZM, Liu RL, Jia BH, Zhang ZF, Wang GC (2010) The Permian lithofacies paleogeographic characteristics and basin-mountain conversion in the Kunlun orogenic belt (in Chinese with English abstract). Geol China 37(2):374–393

Class C, Miller DM, Goldstein SL, Langmuir CH (2000) Distinguishing melt and fluid subduction components in Umnak Volcanics, Aleutian Arc. G^3 1(6):1004. doi:10.1029/1999GC000010

Corfu F, Hanchar JM, Hoskin PWO, Kinny P (2003) Atlas of zircon textures. Rev Mineral Geoche 53(1):469–500

Crawford AJ, Falloon TJ, Eggins S (1987) The origin of island arc high-alumina basalts. Contrib Mineral Petrol 97(3):417–430

Danyushevsky LV (2001) The effect of small amounts of H_2O on crystallisation of mid-ocean ridge and backarc basin magmas. J Volcanol Geoth Res 110(3–4):265–280

Davies JH, von Blanckenburg F (1995) Slab breakoff: a model of lithosphere detachment and its test in the magmatism and deformation of collisional orogens. Earth Planet Sci Lett 129(1–4):85–102

Dokuz A (2011) A slab detachment and delamination model for the generation of carboniferous high-potassium I-type magmatism in the Eastern Pontides, NE Turkey: the Köse composite pluton. Gondwana Res 19(4):926–944

Duretz T, Gerya TV, May DA (2011) Numerical modelling of spontaneous slab breakoff and subsequent topographic response. Tectonophysics 502(1–2):244–256

Elhlou S, Belousova E, Griffin WL, Pearson NJ, O'Reilly SY (2006) Trace element and isotopic composition of GJ-red zircon standard by laser ablation. Geochim Cosmochim Acta 70:A158

Elliott T, Plank T, Zindler A, White W, Bourdon B (1997) Element transport from slab to volcanic front at the Mariana arc. J Geophys Res 102(B7):14991–15019. doi:10.1029/97JB00788

Feng YM, Cao XZ, Zhang EP, Hu YX, Pan XP, Yang JL, Jia QZ, Li WM (2002) Structure, orogenic processes and geodynamic of the western Qinling orogen (in Chinese). Xi'an map press, Xi'an, pp 1–263

Fisher CM, Hanchar JM, Samson SD, Dhuime B, Blichert-Toft J, Vervoort JD, Lam R (2011) Synthetic zircon doped with hafnium and rare earth elements: a reference material for in situ hafnium isotope analysis. Chem Geol 286(1–2):32–47

Gao S, Rudnick RL, Yuan HL, Liu XM, Liu YS, Xu WL, Ling WL, Ayers J, Wang XC, Wang QH (2004) Recycling lower continental crust in the North China craton. Nature 432(7019):892–897

Gerya TV, Yuen DA, Maresch WV (2004) Thermomechanical modelling of slab detachment. Earth Planet Sci Lett 226(1–2): 101–116

Griffin WL, Wang X, Jackson SE, Pearson NJ, O'Reilly SY, Xu X, Zhou X (2002) Zircon chemistry and magma mixing, SE China: in situ analysis of Hf isotopes, Tonglu and Pingtan igneous complexes. Lithos 61(3):237–269

Hawkesworth CJ, Turner SP, McDermott F, Peate DW, Van Calsteren P (1997) U–Th isotopes in arc magmas: implications for element transfer from the subducted crust. Science 276(5312):551

Hu ZC, Liu YS, Gao S, Liu WG, Zhang W, Tong XR, Lin L, Zhou L, Zong KQ, Chen HH (2012) Improved in situ Hf isotope ratio analysis of zircon using newly designed X skimmer cone and jet sample cone in combination with the addition of nitrogen by laser ablation multiple collector ICP-MS. J Anal At Spectrom (in review)

Huppert HE, Sparks RSJ (1988) The generation of granitic magmas by intrusion of basalt into continental crust. J Petrol 29(3):599–624

IUPAC (1991) Isotopic compositions of the elements 1989. J Phys Chem Ref Data (USA) 20(6):1327–1337

Jiang YH, Jin GD, Liao SY, Zhou Q, Zhao P (2010) Geochemical and Sr–Nd–Hf isotopic constraints on the origin of Late Triassic granitoids from the Qinling orogen, central China: implications for a continental arc to continent–continent collision. Lithos 117(1–4):183–197

Jin WJ, Zhang Q, He DF, Jia XQ (2005) SHRIMP dating of adakites in western Qinling and their implications (in Chinese with English abstract). Acta Petrol Sin 21(3):959–966

Johnson MC, Plank T (1999) Dehydration and melting experiments constrain the fate of subducted sediments. G^3 1(12):1007–1026. doi:10.1029/1999GC000014

Kamei A, Owada M, Nagao T, Shiraki K (2004) High-Mg diorites derived from sanukitic HMA magmas, Kyushu Island, southwest Japan arc: evidence from clinopyroxene and whole rock compositions. Lithos 75:359–371

Kelemen PB, Hanghoj K, Greene AR (2003) One view of the geochemistry of subduction-related magmatic arcs, with an emphasis on primitive andesite and lower crust. Treatise Geochem 3:593–659

Kemp A, Hawkesworth CJ, Foster GL, Paterson BA, Woodhead JD, Hergt JM, Gray CM, Whitehouse MJ (2007) Magmatic and crustal differentiation history of granitic rocks from Hf–O isotopes in zircon. Science 315(5814):980–983

Kemp A, Foster GL, Scherstén A, Whitehouse MJ, Darling J, Storey C (2009) Concurrent Pb–Hf isotope analysis of zircon by laser ablation multi-collector ICP-MS, with implications for the crustal evolution of Greenland and the Himalayas. Chem Geol 261(3–4):244–260

Konstantinovskaia EA, Brunel M, Malavieille J (2003) Discovery of the Paleo-Tethys residual peridotites along the Anyemaqen-KunLun suture zone (North Tibet). Comptes Rendus Geosci 335(8):709–719

Koteas GC, Williams ML, Seaman SJ, Dumond G (2010) Granite genesis and mafic-felsic magma interaction in the lower crust. Geology 38(12):1067–1070

Lai SC, Qin JF, Chen L, Grapes R (2008) Geochemistry of ophiolites from the Mian-Lue Suture Zone: implications for the tectonic evolution of the Qinling Orogen, Central China. Int Geol Rev 50(7):650–664

Li SG, Sun WD, Zhang GW, Chen JY, Yang Y (1996) Chronology and geochemistry of metavolcanic rocks from Heigouxia Valley in the Mian-Lue tectonic zone, South Qinling-evidence for a Paleozoic oceanic basin and its close time. Sci China (Ser D) 39:300–310

Li LG, Liao XH, Fu RS (2002) Slab breakoff depth: a slowdown subduction model. Geophys Res Lett 29(3):1041. doi:10.1029/2001GL013420

Li ZC, Pei XZ, Ding SP, Liu ZQ, Wang F, Li GY, Li RB, Li FJ (2007) Zircon U–Pb dating of the Nanyili granodiorite in the Pingwu area, northwestern Sichun, and its geological significance (in Chinese with English abstract). Geol China 34(6):1003–1012

Liu YS, Zong KQ, Kelemen PB, Gao S (2008) Geochemistry and magmatic history of eclogites and ultramafic rocks from the Chinese continental scientific drill hole: subduction and ultra-high-pressure metamorphism of lower crustal cumulates. Chem Geol 247(1–2):133–153

Liu YS, Gao S, Hu ZC, Gao CG, Zong KQ, Wang DB (2010) Continental and oceanic crust recycling-induced melt-peridotite interactions in the Trans-North China Orogen: U–Pb dating, Hf isotopes and trace elements in zircons from mantle xenoliths. J Petrol 51(1–2):537–571

Ludwig KR (2003) Isoplot/Ex version 3.00: a geochronological toolkit for Microsoft Excel. Berkeley Geochronology Center Special Publication, 4:1–73

Mahéo G, Blichert-Toft J, Pin C, Guillot S, Pecher A (2009) Partial melting of mantle and crustal sources beneath south Karakorum, Pakistan: implications for the miocene geodynamic evolution of the India-Asia convergence zone. J Petrol 50(3):427–449

Massonne HJ (2005) Involvement of crustal material in delamination of the lithosphere after continent–continent collision. Int Geol Rev 47(8):792–804

Meng QR, Zhang GW (1999) Timing of collision of the North and South China blocks: controversy and reconciliation. Geology 27(2):123–126

Meng QR, Zhang GW (2000) Geologic framework and tectonic evolution of the Qinling orogen, central China. Tectonophysics 323(3–4):183–196

Meng QR, Wang E, Hu JM (2005) Mesozoic sedimentary evolution of the northwest Sichuan basin: implication for continued clockwise rotation of the South China block. Geol Soc Am Bull 117(3–4):396–410

Moyen JF, Stevens G (2006) Experimental constraints on TTG petrogenesis: implications for Archean geodynamics. Archean Geodyn Environ 164:1–28

Pearce JA, Peate DW (1995) Tectonic implications of the composition of volcanic arc magmas. Ann Rev Earth Planet Sci Lett 23:251–286

Peccerillo A, Taylor SR (1976) Geochemistry of eocene calc-alkaline volcanic rocks from the Kastamonu area, northern Turkey. Contrib Mineral Petrol 58(1):63–81

Qin JF, Lai SC, Li YF (2008) Slab breakoff model for the Triassic post-collisional adakitic granitoids in the Qinling Orogen, central China: zircon U–Pb ages, geochemistry, and Sr–Nd–Pb isotopic constraints. Int Geol Rev 50(12):1080–1104

Qin JF, Lai SC, Grapes R, Diwu CR, Ju YJ, Li YF (2009) Geochemical evidence for origin of magma mixing for the Triassic monzonitic granite and its enclaves at Mishuling in the Qinling orogen (central China). Lithos 112(3–4):259–276

Qin JF, Lai SC, Diwu CR, Ju YJ, Li YF (2010a) Magma mixing origin for the post-collisional adakitic monzogranite of the Triassic Yangba pluton, Northwestern margin of the South China block: geochemistry, Sr–Nd isotopic, zircon U–Pb dating and Hf isotopic evidences. Contrib Mineral Petrol 159(3):389–409

Qin JF, Lai SC, Grapes R, Diwu CR, Ju YJ, Li YF (2010b) Origin of Late Triassic high-Mg adakitic granitoid rocks from the

Dongjiangkou area, Qinling orogen, central China: implications for subduction of continental crust. Lithos 120(3–4):347–367

Rapp RP, Watson EB (1995) Dehydration melting of metabasalt at 8–32 kbar: implications for continental growth and crust-mantle recycling. J Petrol 36(4):891–931

Rapp RP, Shimizu N, Norman MD, Applegate GS (1999) Reaction between slab-derived melts and peridotite in the mantle wedge; experimental constraints at 3.8 GPa. Chem Geol 160(4):335–356

Ratschbacher L, Hacker BR, Calvert A, Webb LE, Grimmer JC, McWilliams MO, Ireland T, Dong S, Hu J (2003) Tectonics of the Qinling (Central China): tectonostratigraphy, geochronology, and deformation history. Tectonophysics 366(1–2):1–53

Ren JS (2004) Some problems on the Kunlun–Qinling orogenic system (in Chinese with English abstract). Northwest Geol 37(1):1–5

Roberts MP, Clemens JD (1993) Origin of high-potassium, calc-alkaline, I-type granitoids. Geology 21(9):825–828

Rogers RD, Kárason H, Van Der Hilst RD (2002) Epeirogenic uplift above a detached slab in northern Central America. Geology 30(11):1031

Rushmer T (1991) Partial melting of two amphibolites: contrasting experimental results under fluid-absent conditions. Contrib Mineral Petrol 107(1):41–59

Scherer E, Münker C, Mezger K (2001) Calibration of the lutetium–hafnium clock. Science 293(5530):683–687

Sisson TW, Grove TL (1993) Temperatures and H_2O contents of low-MgO high-alumina basalts. Contrib Mineral Petrol 113(2):167–184

Sisson TW, Ratajeski K, Hankins WB, Glazner AF (2005) Voluminous granitic magmas from common basaltic sources. Contrib Mineral Petrol 148(6):635–661

Sun SS, McDonough WF (1989) Chemical and isotopic systematics of oceanic basalts: implications for mantle composition and processes. In: Sunders AD, Norry MJ (eds) Magmatism in the ocean basins. Special Publications, London 42:313–345

Sun WD, Li SG, Chen YD, Li YJ (2002) Timing of synorogenic granitoids in the South Qinling, Central China: constraints on the evolution of the Qinling–Dabie orogenic belt. J Geol 110(4):457–468

Tatsumi Y (2006) High-Mg andesites in the Setouchi Volcanic Belt, Southwestern Japan: analogy to archean magmatism and continental crust formation? Annu Rev Earth Planet Sci 34:467–499

Tepper JH, Kuehner SM (2004) Geochemistry of mafic enclaves and host granitoids from the Chilliwack Batholith, Washington: chemical exchange processes between coexisting mafic and felsic magmas and implications for the interpretation of enclave chemical traits. J Geol 112(3):349–367

Tepper JH, Nelson BK, Bergantz GW, Irving AJ (1993) Petrology of the Chilliwack batholith, North Cascades, Washington: generation of calc-alkaline granitoids by melting of mafic lower crust with variable water fugacity. Contrib Mineral Petrol 113(3):333–351

Valley PM, Fisher CM, Hanchar JM, Lam R, Tubrett M (2010) Hafnium isotopes in zircon: a tracer of fluid–rock interaction during magnetite–apatite (“Kiruna-type”) mineralization. Chem Geol 275(3–4):208–220

van de Flierdt T, Hoernes S, Jung S, Masberg P, Hoffer E, Schaltegger U, Friedrichsen H (2003) Lower crustal melting and the role of open-system processes in the genesis of syn-orogenic quartz diorite–granite–leucogranite associations: constraints from Sr–Nd–O isotopes from the Bandombaai Complex, Namibia. Lithos 67(3–4):205–226

Van de Zedde D, Wortel M (2001) Shallow slab detachment as a transient source of heat at midlithospheric depths. Tectonics 20(6):868–882

Vervoort JD, Blichert-Toft J (1999) Evolution of the depleted mantle: Hf isotope evidence from juvenile rocks through time. Geochim Cosmochim Acta 63(3–4):533–556

Wagner TP, Donnelly-Nolan JM, Grove TL (1995) Evidence of hydrous differentiation and crystal accumulation in the low-MgO, high-Al_2O_3 Lake Basalt from Medicine Lake volcano, California. Contrib Mineral Petrol 121:201–216

Wang YB, Huang JC, Luo MS, Tian J, Bai YS (1997) Paleo-Ocean evolution of the southern eastern Kunlun Orogenic belt during Hercy-Early Indosinian (in Chinese with English abstract). J Chin Univ Geosci 22(4):369–372

Wang HQ, Zhu YH, Lin QX, Li XL, Wang K (2010) LA-ICP-MS zircon U–Pb dating of the gabbro from Longwu Gorge ophiolite, Jianzha-Tongren area, Qinghai, China and its geological significance (in Chinese with English abstract). Geol Bull China 29(1):86–92

Wolf MB, Wyllie PJ (1994) Dehydration-melting of amphibolite at 10 kbar: the effects of temperature and time. Contrib Mineral Petrol 115(4):369–383

Woodhead JD, Hergt JM (2005) A preliminary appraisal of seven natural zircon reference materials for in situ Hf isotope determination. Geostand Geoanal Res 29(2):183–195

Woodhead J, Hergt J, Shelley M, Eggins S, Kemp R (2004) Zircon Hf-isotope analysis with an excimer laser, depth profiling, ablation of complex geometries, and concomitant age estimation. Chem Geol 209(1–2):121–135

Wortel MJR, Spakman W (2000) Subduction and slab detachment in the Mediterranean–Carpathian region. Science 290(5498):1910–1917

Wu FY, Huang BC, Ye K, Fang AM (2008) Collapsed Himalayan-Tibetan orogen and the rising Tibetan Plateau (in Chinese with English abstract). Acta Petrol Sin 24(1):1–30

Xu J, Castillo PR, Li X, Yu X, Zhang B, Han Y (2002) MORB-type rocks from the Paleo-Tethyan Mian-Lueyang northern ophiolite in the Qinling Mountains, central China: implications for the source of the low $^{206}Pb/^{204}Pb$ and high $^{143}Nd/^{144}Nd$ mantle component in the Indian Ocean. Earth Planet Sci Lett 198(3–4):323–337

Yang LP (2008) Genesis of Skarn in Xiekeng copper and gold deposits, Xunhua County, Qinghai Province (in Chinese with English abstract). Master Thesis, China Univ Geosci, Beijing, pp 1–83

Yang JH, Wu FY, Wilde SA, Xie LW, Yang YH, Liu XM (2007) Tracing magma mixing in granite genesis: in situ U–Pb dating and Hf-isotope analysis of zircons. Contrib Mineral Petrol 153(2):177–190

Yang JS, Shi RD, Wu CL, Wang XB, Robinson PT (2009) Dur’ngoi ophiolite in East Kunlun, Northeast Tibetan plateau: evidence for paleo-Tethyan suture in Northwest China. J Earth Sci 20(2):303–331

Yin HF, Zhang KX (1998) Evolution and characteristics of the Central Orogenic Belt (in Chinese with English abstract). J China Univ Geosci 23(5):438–442

Yin HF, Yang FQ, Huang QS, Lai SL, Yang HS (1992) The Triassic of Qinling mountains (in Chinese with English abstract). China Univ Geosci Press, Wuhan, pp 1–211

Yuan HL, Gao S, Dai MN, Zong CL, Günther D, Fontaine GH, Liu XM, Diwu CR (2008) Simultaneous determinations of U–Pb age, Hf isotopes and trace element compositions of zircon by excimer laser-ablation quadrupole and multiple-collector ICP-MS. Chem Geol 247(1–2):100–118

Zhang GW, Zhang BR, Yuan XC, Chen JY (2001) Qinling Orogenic Belt and continental dynamics (in Chinese with English abstract). Science Press, Beijing, pp 1–855

Zhang HF, Gao S, Zhong ZQ, Zhang BR, Zhang L, Hu SH (2002) Geochemical and Sr–Nd–Pb isotopic compositions of Cretaceous granitoids: constraints on tectonic framework and crustal structure of the Dabieshan ultrahigh-pressure metamorphic belt, China. Chem Geol 186(3–4):281–299

Zhang HF, Cheng YL, Xu WC, Liu R, Yuan HL, Liu XM (2006) Granitoids around Gonghe basin in Qinghai province: petrogenesis and tectonic implications (in Chinese with English abstract). Acta Petrol Sin 22(12):2910–2922

Zhang HF, Jin LL, Zhang L, Harris N (2007a) Geochemical and Pb–Sr–Nd isotopic compositions of granitoids from western Qinling belt: constraints on basement nature and tectonic affinity. Sci China (Ser D) 50:184–196

Zhang HF, Xiao L, Zhang L (2007b) Geochemical and Pb–Sr–Nd isotopic compositions of Indosinian granitoids from the Bikou block, northwest of the Yangtze plate: constraints on petrogenesis, nature of deep crust and geodynamics. Sci China (Ser D) 50(7):972–983

Zhang CL, Wang T, Wang XX (2008) Origin and tectonic setting of the Early Mesozoic Granitoids in Qinling Orogenic Belt (in Chinese with English abstract). Geol J China Univ 14(3):304–316

Zheng DW, Zhang PZ, Wan JL, Li DM, Wang F, Yuan DY, Zhang GL (2004) The ^{40}Ar/^{39}Ar, fission track evidence of Mesozoic tectonic in northern margin of west Qinling mountain (in Chinese with English abstract). Acta Petrol Sin 20(3):697–706

Zheng YF, Zhao ZF, Wu YB, Zhang SB, Liu X, Wu FY (2006) Zircon U–Pb age, Hf and O isotope constraints on protolith origin of ultrahigh-pressure eclogite and gneiss in the Dabie orogen. Chem Geol 231(1–2):135–158

Zheng JP, Griffin WL, Sun M, O'Reilly SY, Zhang HF, Zhou HW, Xiao L, Tang HY, Zhang ZH (2010) Tectonic affinity of the west Qinling terrane (central China): North China or Yangtze? Tectonics 29(2):TC2009